Neuron

Article

GluN3A excitatory glycine receptors control adult cortical and amygdalar circuits

Graphical abstract

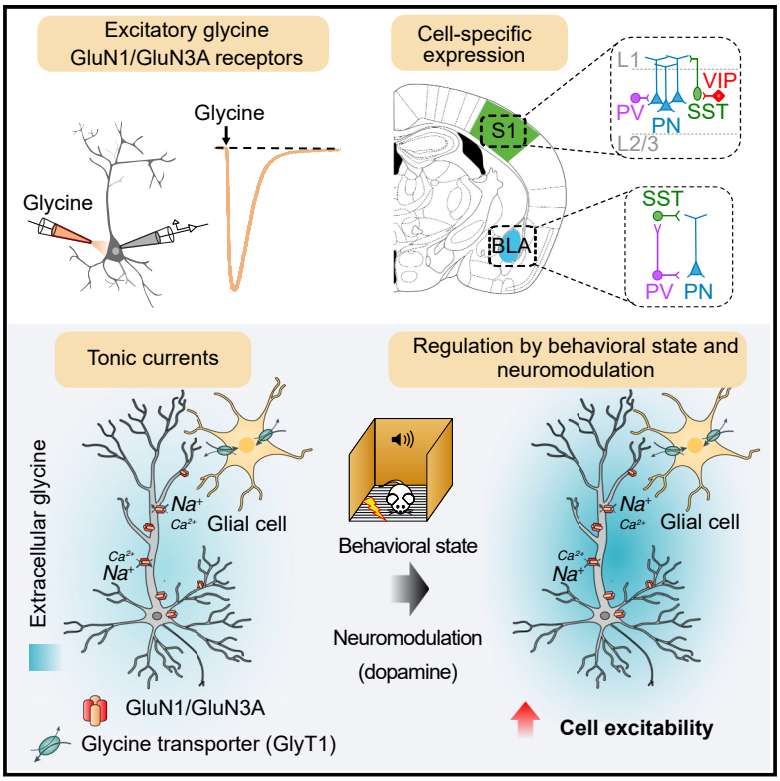

Highlights

- In mice, GluN3A is expressed by SST-INs in the cortex and pyramidal neurons in the BLA
- GluN3A assembles as excitatory glycine GluN1/GluN3A receptors (eGlyRs)
- eGlyRs detect extracellular glycine levels and generate tonic excitatory currents
- eGlyRs tune the function of SST-INs in cortex and alter the formation of fear memories in BLA

Authors

Simon Bossi, Dhanasak Dhanasobhon, Graham C.R. Ellis-Davies, ..., Daniela Popa, Pierre Paoletti, Nelson Rebola

Correspondence

pierre.paoletti@ens.psl.eu (P.P.), nelson.rebola@icm-institute.org (N.R.)

In brief

Bossi et al. show that GluN3A subunits control the activity of selective neuronal populations in the adult mouse brain via the formation of excitatory glycine GluN1/GluN3A receptors (eGlyRs). Functional analysis reveals that eGlyRs regulate the recruitment of somatostatin-positive interneurons in the neocortex and participate in the stability of fear memories in the BLA.

Bossi et al., 2022, Neuron *110*, 2438–2454
August 3, 2022 © 2022 The Authors. Published by Elsevier Inc.
https://doi.org/10.1016/j.neuron.2022.05.016

CellPress

CellPress
OPEN ACCESS

Neuron

Article

GluN3A excitatory glycine receptors control adult cortical and amygdalar circuits

Simon Bossi,[1,7] Dhanasak Dhanasobhon,[2,7] Graham C.R. Ellis-Davies,[3] Jimena Frontera,[1] Marcel de Brito Van Velze,[2] Joana Lourenço,[2] Alvaro Murillo,[5,6] Rafael Luján,[4] Mariano Casado,[1] Isabel Perez-Otaño,[5] Alberto Bacci,[2] Daniela Popa,[1] Pierre Paoletti,[1,7,8,*] and Nelson Rebola[2,7,8,9,*]

[1]Institut de Biologie de l'Ecole Normale Supérieure (IBENS), Ecole Normale Supérieure, Université PSL, CNRS, INSERM, F-75005 Paris, France

[2]Sorbonne Université, Institut Du Cerveau-Paris Brain Institute-ICM, Inserm U1127, CNRS UMR 7225, 47 Boulevard de l'Hôpital, 75013 Paris, France

[3]Department of Neuroscience, Mount Sinai School of Medicine, One Gustave Levy Place, New York, NY 10029, USA

[4]Synaptic Structure Laboratory, Instituto de Investigación en Discapacidades Neurológicas (IDINE), Facultad de Medicina, Universidad Castilla-La Mancha, 02006 Albacete, Spain

[5]Instituto de Neurociencias (CSIC-UMH), San Juan de Alicante 03550, Spain

[6]Present address: UK Dementia Research Institute at Cardiff University, CF24 4HQ Cardiff, UK

[7]These authors contributed equally

[8]Senior author

[9]Lead contact

*Correspondence: pierre.paoletti@ens.psl.eu (P.P.), nelson.rebola@icm-institute.org (N.R.)

https://doi.org/10.1016/j.neuron.2022.05.016

SUMMARY

GluN3A is an atypical glycine-binding subunit of NMDA receptors (NMDARs) whose actions in the brain are mostly unknown. Here, we show that the expression of GluN3A subunits controls the excitability of mouse adult cortical and amygdalar circuits via an unusual signaling mechanism involving the formation of excitatory glycine GluN1/GluN3A receptors (eGlyRs) and their tonic activation by extracellular glycine. eGlyRs are mostly extrasynaptic and reside in specific neuronal populations, including the principal cells of the basolateral amygdala (BLA) and SST-positive interneurons (SST-INs) of the neocortex. In the BLA, tonic eGlyR currents are sensitive to fear-conditioning protocols, are subject to neuromodulation by the dopaminergic system, and control the stability of fear memories. In the neocortex, eGlyRs control the *in vivo* spiking of SST-INs and the behavior-dependent modulation of cortical activity. GluN3A-containing eGlyRs thus represent a novel and widespread signaling modality in the adult brain, with attributes that strikingly depart from those of conventional NMDARs.

INTRODUCTION

In the brain, NMDA receptors (NMDARs) represent a particular type of membrane receptors specialized in the detection of the excitatory neurotransmitter glutamate (Glu) using glycine or D-serine as a co-agonist (Johnson and Ascher, 1987; Kleckner and Dingledine, 1988; Traynelis et al., 2010). The vast majority of the reported actions of NMDARs, including their well-established role as key drivers of long-term synaptic plasticity (Nicoll, 2017), are mediated by the formation of tetrameric assemblies between mandatory glycine (or D-serine)-binding GluN1 subunits and Glu-binding GluN2 subunits (GluN2A-D; Paoletti et al., 2013; Traynelis et al., 2010). Simultaneous binding of Glu and glycine or D-serine is required for GluN1/GluN2 NMDAR activation (Johnson and Ascher, 1987; Kleckner and Dingledine, 1988; Stroebel et al., 2021). In heterologous expression systems, however, the exclusivity of such a ubiquitous model has been challenged by the report that GluN1 subunits could co-assemble with GluN3 subunits to form functional channels gated by glycine only (Awobuluyi et al., 2007; Chatterton et al., 2002; Madry et al., 2007; Ulbrich and Isacoff, 2008). GluN1/GluN3A glycine-gated NMDARs do not respond to Glu and are insensitive to classical NMDAR antagonists like D-AP5 or MK-801 (Awobuluyi et al., 2007; Chatterton et al., 2002; Madry et al., 2007). For long, however, the existence of such excitatory glycine receptors (eGlyRs) in the CNS has remained undefined.

Recently, functional GluN1/GluN3A receptors have been reported in the neurons of the juvenile hippocampus (Grand et al., 2018) and adult medial habenula where they participate in the control of aversive behaviors (Otsu et al., 2019). However, the expression of GluN3A in the adult brain far exceeds this latter region, as evidenced by early (Ciabarra et al., 1995; Sucher et al., 1995) and recent (Murillo et al., 2021; Paul et al., 2017) mRNA studies showing sustained GluN3A expression levels in multiple regions and cell types. The expression of GluN3A subunits is particularly evident in forebrain regions like the neocortex

 © 2022 The Authors. Published by Elsevier Inc.
This is an open access article under the CC BY-NC-ND license (http://creativecommons.org/licenses/by-nc-nd/4.0/).

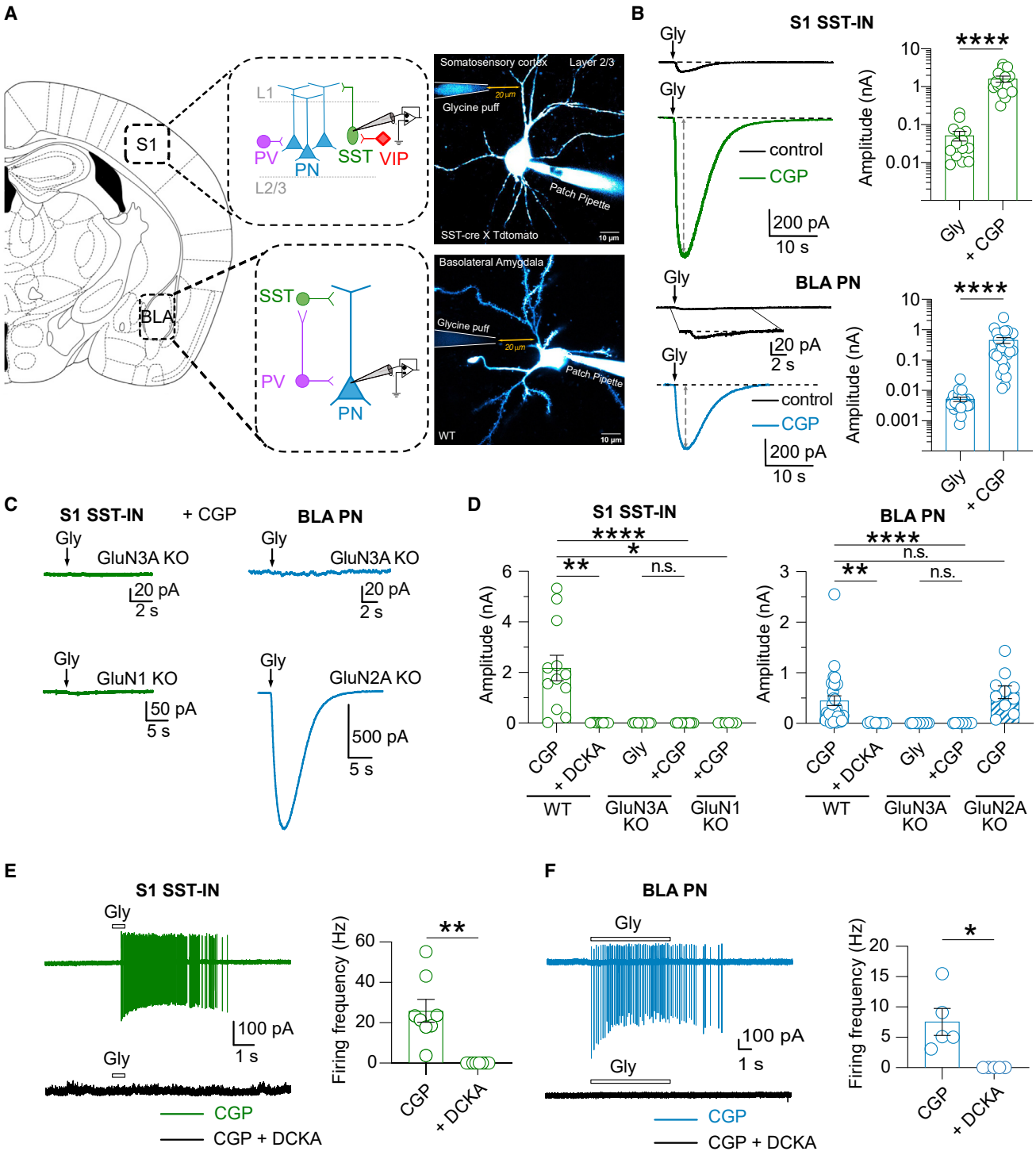

Figure 1. Functional expression of eGlyRs in adult amygdala and neocortex

(A) Schematic representation of the canonical cellular organization of S1 and BLA microcircuits. Right: two-photon laser scanning microscopy (2PLSM) images of a patched cortical SST-IN in S1 and a PN in the BLA with the location of the glycine puff pipette.

(B) Sample traces and peak amplitudes of glycine (10 mM)-puff-evoked inward currents in S1 SST-INs (n = 15) and BLA PNs (n = 29) in control conditions and after the bath application of CGP-78608 (1–2 μM; ****p < 0.0001, Wilcoxon signed-rank test).

(C and D) Same as (B) but for the brain slices from GluN3A KO mice (S1, WT [n = 12] versus GluN3A KO [n = 10], p < 0.0001; BLA, WT [n = 29] versus GluN3A KO [n = 11], p < 0.0001) or after the bath application of DCKA (S1: control [n = 12] versus DCKA [n = 12], p = 0.0112; BLA: control [n = 29] versus DCKA [n = 8],

(legend continued on next page)

and the basolateral amygdala (BLA) (Murillo et al., 2021; Paul et al., 2017; Pfeffer et al., 2013). These observations suggest that eGlyRs might have a broader presence and action in the brain than previously anticipated. Intriguingly, GluN3A subunits populate brain areas almost completely devoid of glycinergic innervation (Zeilhofer et al., 2005), raising the question about the potential native signals that drive GluN1/GluN3A receptor activation. In the medial habenula, chemogenetic-assisted stimulation of astrocytes results in increased eGlyR activity, suggesting the involvement of glial cells (Otsu et al., 2019). However, the endogenous signals that control eGlyR activity and how the recruitment of such atypical receptors contributes to brain function remain largely unknown. Moreover, GluN3A is generally thought to act as a modulatory subunit of conventional NMDARs, altering their biophysical properties through the formation of Glu-sensitive triheteromeric GluN1/GluN2/GluN3A receptor complexes (Al-Hallaq et al., 2002; Das et al., 1998; Perez-Otano et al., 2001; Pérez-Otaño et al., 2016; Roberts et al., 2009; Sasaki et al., 2002; Tong et al., 2008). It is, therefore, difficult to predict how widespread GluN1/GluN3A receptors are and how this unusual NMDAR subtype controls the neuronal function in the adult brain. Using a multi-scale approach, we now reveal that GluN3A subunits lead to the selective formation of diheteromeric GluN1/GluN3A receptors in specific cell populations in the neocortical and amygdalar microcircuits. In the somatostatin-positive interneurons (SST-INs) in the neocortex as well as the pyramidal cells in the BLA, we show that eGlyRs are the dominant population of receptors formed by GluN3A subunits with no evidence for functional triheteromeric (GluN1/GluN2/GluN3A) assemblies. We demonstrate that eGlyRs control neuronal excitability by acting as sensors of endogenous glycine levels. We also observe that tonic eGlyR activity is plastic, being regulated by the animal behavioral state and the neuromodulator dopamine. Our results identify eGlyRs as a new signaling system present in multiple brain regions by which extracellular glycine tunes neuronal activity, circuit function, and behavior.

RESULTS

GluN3A subunits form eGlyRs in both the amygdala and the neocortex

In the neocortex, GluN3A subunits seem to be particularly abundant in GABAergic SST-INs (Murillo et al., 2021; Paul et al., 2017; Pfeffer et al., 2013), whereas in the BLA, a cortex-like structure, their expression is abundant in pyramidal neurons (PNs; Figure S1A). We decided to explore this complementary expression pattern in order to dissect the cellular mechanisms by which GluN3A impacts the activity of single neurons in the adult brain. We initially tested whether the expression of GluN3A subunits is associated with the presence of unusual glycine-gated GluN1/GluN3A receptors.

To probe for eGlyRs, we first patch clamped both SST-INs in the primary somatosensory cortex (S1 SST-INs) and glutamatergic PNs in the BLA (BLA PNs) and recorded the responses to pressure-applied glycine (10 mM) in the presence of a cocktail of receptor antagonists against most ionotropic glutamatergic, glycinergic, and GABAergic receptors (see STAR Methods). Small glycine-evoked excitatory currents were observed (Figures 1A and 1B), suggesting the presence of eGlyRs in both brain regions. Repeating glycine puff applications in the presence of the GluN1 antagonist CGP-78608, which strongly reduces GluN1/GluN3A receptor desensitization (Grand et al., 2018; Otsu et al., 2019), resulted in currents that frequently reached the nA range in both cell types (Figures 1B–1D). Current-voltage (I-V) curves of glycine-evoked currents, both in the presence and in the absence of CGP-78608, displayed only modest outward rectification contrasting with classical GluN1/GluN2 NMDARs but fully compatible with the gating of GluN1/GluN3A receptors (Chatterton et al., 2002; Otsu et al., 2019) (Figures S1B and S1C). We examined further whether the recorded currents were indeed mediated by GluN1/GluN3A receptor assemblies. As expected, the pharmacological application of 5,7-dichlorokynurenic acid (DCKA) (500 μM), a dual GluN1 and GluN3 glycine-binding site antagonist (Awobuluyi et al., 2007; Chatterton et al., 2002), completely abolished glycine-evoked responses (Figure 1D). Similarly, no currents were observed when the experiments were repeated (with or without CGP-78608) in the brain slices from GluN3A KO animals (Das et al., 1998) in both S1 SST-INs and BLA PNs (Figures 1C and 1D). The selective removal of GluN1 subunits from S1 SST-INs also resulted in the elimination of pressure-evoked glycine currents in this particular interneuron subtype (Figures 1C and 1D). By contrast, glycinergic currents remained unaltered in the BLA neurons recorded from animals lacking GluN2A, a Glu-binding NMDAR subunit widely expressed in the adult forebrain (Figures 1C and 1D). We then studied the effect of GluN1/GluN3A-mediated currents on cell discharge activity using cell-attached recordings. Glycine puff applications in the presence of CGP-78608 induced robust and sustained spiking of both S1 SST-INs and BLA PNs (Figures 1E and 1F). Overall, these results reveal that GluN1/GluN3A receptors are functionally expressed at high density in different neuronal territories of the adult brain where they mediate a depolarizing action when activated by glycine. Spurred by these initial results, we decided to pursue our dual brain region approach (BLA and S1), aiming to unravel general working principles of eGlyRs.

eGlyRs are cell-type specific and constitute the main receptor assembly formed by GluN3A subunits

Despite their distribution across multiple brain regions, we noticed that GluN1/GluN3A-mediated currents were not homogeneous across different neuronal cell populations. In the neocortex, glycine-evoked currents were mostly restricted to

p = 0.0046). Glycine-evoked currents are also absent in the GluN1 lacking S1 SST-INs (GluN1 KO; n = 7, p = 0.00313). By contrast, removing GluN2A subunits does not affect the glycine-evoked currents in the BLA (GluN2A KO; n = 10; p > 0.99 Kruskal-Wallis followed by Dunn's multiple comparisons test).

(E) In S1 SST-INs, the puffs of glycine (10 mM) elicit action potential firing in the presence of CGP-78608 (1–2 μM), an effect antagonized by DCKA (500 μM) application (n = 8, p = 0.0026, paired t test).

(F) Same as (E) but for BLA PNs (n = 5, p = 0.0271, paired t test).

(B, D, E, and F) Bars indicate mean ± SEM.

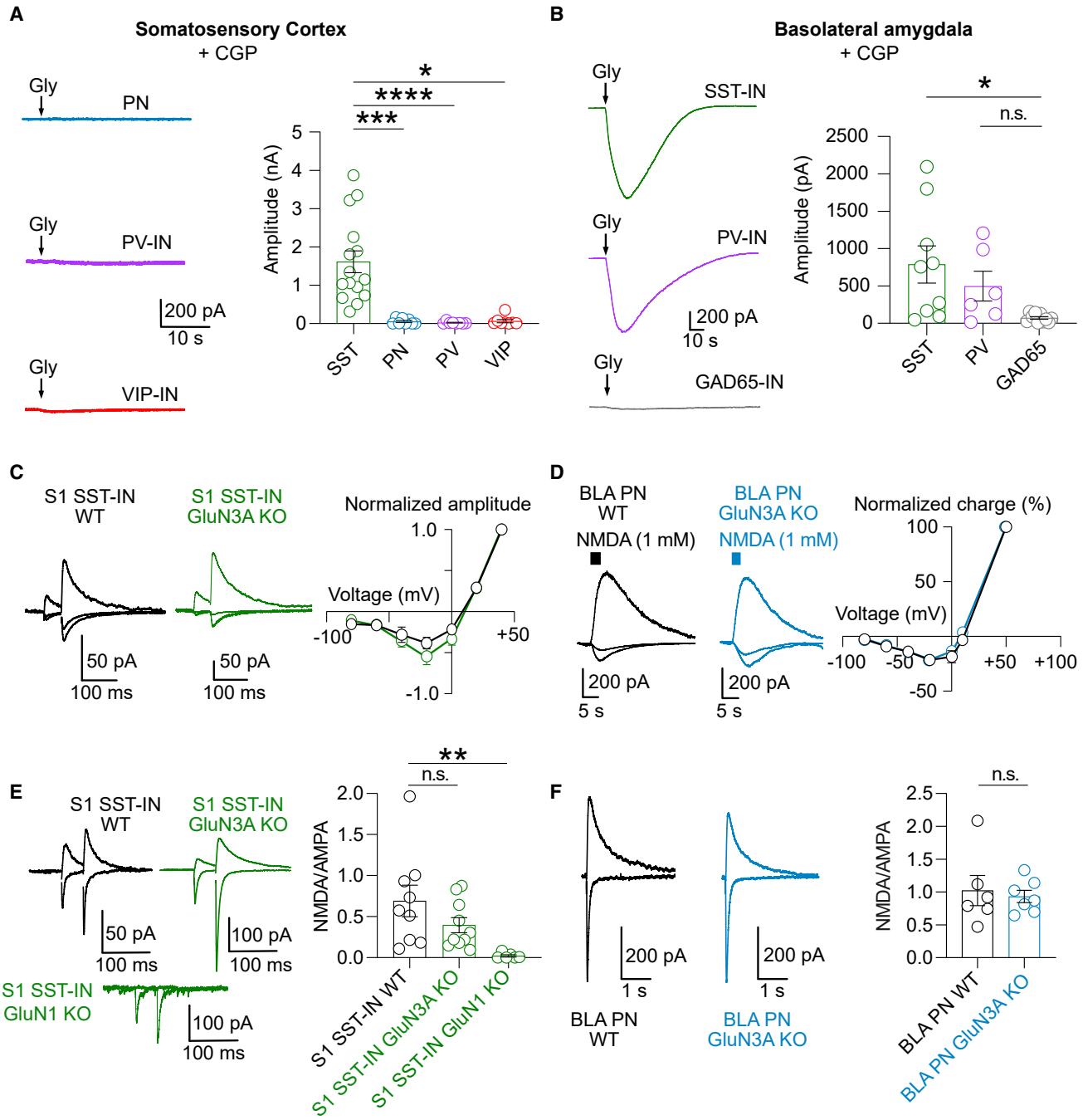

Figure 2. eGlyR expression is cell specific, and GluN3A subunits mainly form diheteromeric GluN1/GluN3A complexes in adult cortical and BLA neurons

(A) Representative traces and amplitudes of glycine (10 mM)-evoked currents in S1 neurons in the presence of CGP-78608 (1–2 μM). Note the particular enrichment in SST-INs (SST-INs [n = 15] versus PNs [n = 8], p = 0.0001; versus PV-INs [n = 8], p < 0.0001; versus VIP-INs [n = 8], p = 0.0030, Kruskal-Wallis followed by Dunn's multiple comparisons test). Application of CGP-78608 revealed small statistically significant currents in VIP-INs, yet they were considerably smaller than those in SST-INs. No statistically significant currents were detected in PNs and PV-INs.

(B) Same as (A) but for three interneuron populations (SST, PV, and GAD-65) in the BLA (GAD-65 [n = 10]; versus SST-INs [n = 9], p = 0.0059; versus PV-INs [n = 6], p = 0.0786, Kruskal-Wallis followed by Dunn's multiple comparisons test).

(C) Example traces (−60, −20, and +40 mV) and current-voltage relationship of synaptic NMDA-EPSCs from the S1 SST-INs in WT and GluN3A KO mice (−60 mV: WT [n = 8] versus GluN3A KO [n = 7], p = 0.5358; −80 mV: WT [n = 8] versus GluN3A KO [n = 7], p = 0.0721, Mann-Whitney U test). Points represent mean ± SEM.

(legend continued on next page)

SST-INs and not present in L2/3 PNs, parvalbumin (PV) or vasoactive intestinal peptide (VIP) interneurons (Figures 2A and S1D). By contrast, in the BLA, GluN1/GluN3A receptor activity was readily observed in both PNs, PV-Ins, and SST-INs but was absent in GAD65-INs, which label (among others) a population of VIP-INs (Rhomberg et al., 2018) (Figure 2B). Besides assembling with GluN1 subunits into Glu-insensitive diheteromeric GluN1/GluN3A receptors, GluN3A subunits can also assemble as triheteromeric receptors (GluN1/GluN2/GluN3A) with properties closer to classical (Glu-sensitive) NMDARs but displaying a reduction in magnesium block sensitivity (Perez-Otano et al., 2001; Pérez-Otaño et al., 2016). To assess the presence of triheteromeric GluN3A-containing receptors, we examined the I-V relationship of synaptic (Yuan et al., 2013) and puff-evoked (Otsu et al., 2019) NMDAR currents in BLA PNs and S1 SST-INs. The I-V curves of synaptic and puff-evoked NMDAR currents in mice lacking GluN3A subunits were not different from those in control animals (Figures 2C and 2D). Similarly, synaptic AMPA/NMDA current amplitude ratios were indistinguishable between the two genotypes (Figures 2E and 2F). These results indicate that in the adult neocortical SST-INs and BLA PNs, no or very few functional triheteromeric GluN1/GluN2/GluN3A receptors exist. Rather, GluN3A subunits associate mainly, if not exclusively, with GluN1 subunits to form diheteromeric GluN1/GluN3A glycine-gated receptors.

eGlyRs are distributed between synaptic and extrasynaptic subcellular compartments

We next investigated the subcellular distribution of eGlyRs. For this purpose, we synthesized a photolabile derivative of glycine, 4-(carboxymethoxy)-7-nitroindolinyl (CNI)-caged glycine (CNI-Gly; Figures 3A, S2A, and S2B), and used two-photon (2P) imaging and uncaging to map the neuronal distribution of GluN1/GluN3A receptors. We first verified the validity of the newly synthetized caged compound as an efficient light-sensitive source of glycine. In the dorsal horn spinal cord neurons, known to be enriched in inhibitory glycinergic receptors (Legendre, 2001), brief (1–50 ms) 2P uncaging pulses positioned close (<2 μm) to fluorescently labeled neurons in the presence of locally applied CNI-Gly (5 mM) reliably evoked strychnine-sensitive currents (Figures S2C–S2E). We then tested the ability to activate eGlyRs by uncaging glycine. In the presence of a cocktail of receptor antagonists (see STAR Methods), light-emitting diode (LED, 405 nm) CNI glycine illumination resulted in the detection of clear inward currents in the S1 SST-INs from wild-type (WT), but not GluN3A KO, animals (Figures S2F and S2G). We next probed the spatial distribution of GluN1/GluN3A receptors. We performed these experiments in the presence of CGP-78608 to facilitate the detection of eGlyR currents. In agreement with the presence of GluN1/GluN3A receptors, 2P CNI-Gly uncaging evoked inward currents in both S1 SST-INs and BLA PNs that were fully blocked by DCKA (Figures 3B, 3C, and S3A). Light-evoked currents were lost if the uncaging spot was positioned >2 μm away from the targeted neuron, revealing spatially restricted activation of GluN1/GluN3A receptors (Figure S3B). We then compared in BLA PNs (where spines can be easily identified) the amplitude of photolysis-evoked glycine currents while positioning the uncaging spot close to a spine or to the dendritic shaft. We observed no difference in the amplitude of photolysis-evoked currents between the two subcellular compartments, suggesting that in contrast to classical NMDARs (Matsuzaki et al., 2004; Sheng and Kim, 2011), GluN1/GluN3A receptors are not enriched in spines (Figure 3D). As a comparison, the photolysis of 4-Methoxy-7-nitroindolinyl-caged-L-glutamate (MNI-Glu) using similar uncaging durations evoked currents with significantly larger amplitudes in spine than in shaft (Figures 3E and Figures S3C–S3F). We complemented the functional mapping of GluN1/GluN3A receptors with immunoelectron microscopy. In the hippocampus, GluN3A subunits are evenly distributed over the dendritic plasma membrane (Pérez-Otaño et al., 2006). Immunogold quantification selective for the GluN3A subunit in the BLA revealed a similar pattern with a strong enrichment at the cell surface and gold particles shared between synaptic and extrasynaptic regions (slight preference for extrasynaptic regions versus PSD; Figure 3F). Altogether, these data establish that GluN1/GluN3A receptors do not cluster preferentially at dendritic spines but rather have a diffuse distribution across the different neuronal subcellular compartments.

Tonic activation of eGlyRs by endogenous glycine

The lack of enrichment of GluN1/GluN3A receptors in dendritic spines together with their homogeneous distribution in the dendrites suggests that these atypical NMDARs are unlikely to detect localized glycine release. This hypothesis is further supported by the conspicuous scarcity of the glycinergic innervation of both amygdalar and neocortical regions (Zeilhofer et al., 2005). The activating GluN3A subunit has a particularly high affinity for glycine, whereas the desensitizing GluN1 subunit displays lower glycine sensitivity (Awobuluyi et al., 2007; Chatterton et al., 2002; Grand et al., 2018; Madry et al., 2007; Yao and Mayer, 2006). This functional scheme appears particularly well tailored to detect ambient glycine levels found in the brain extracellular space at low micromolar concentrations (Westergren et al., 1994; Zhang et al., 2018). With this premise in mind, we measured the effect of GluN1/GluN3A receptor inhibition on holding (or leak) currents. In amygdala PNs, the application of DCKA in the presence of D-AP5 (to exclude possible confounding effects from conventional NMDARs) shifted leak currents to more positive values (Figures 4A and 4B). This effect was absent

(D) Example traces (−60, −20, and +50 mV) and current-voltage relationship of NMDAR currents elicited by pressure-applied NMDA in the BLA PNs in WT and GluN3A KO mice (−60 mV: WT [n = 5] versus GluN3A KO [n = 6], p = 0.5368; −80 mV: WT [n = 5] versus GluN3A KO [n = 6], p = 0.6623, Mann-Whitney U test). Points represent mean ± SEM.

(E) Example traces and summary plot of synaptic NMDA/AMPA ratio recorded in the S1 SST-INs of WT, GluN3A KO, and SST:GluN1 KO mice. Note that removing GluN3A subunit does not alter the NMDA/AMPA ratio, whereas the loss of GluN1 abolishes NMDAR currents (WT [n = 9] versus GluN3A KO [n = 10], p = 0.7635; versus GluN1 KO [n = 6], p = 0.0006, Kruskal-Wallis followed by Dunn's multiple comparisons test).

(F) Same as (E) but for BLA PNs (WT [n = 6] versus GluN3A KO [n = 7], p = 0.8072, unpaired t test).

(A, B, E, and F) Bars indicate mean ± SEM.

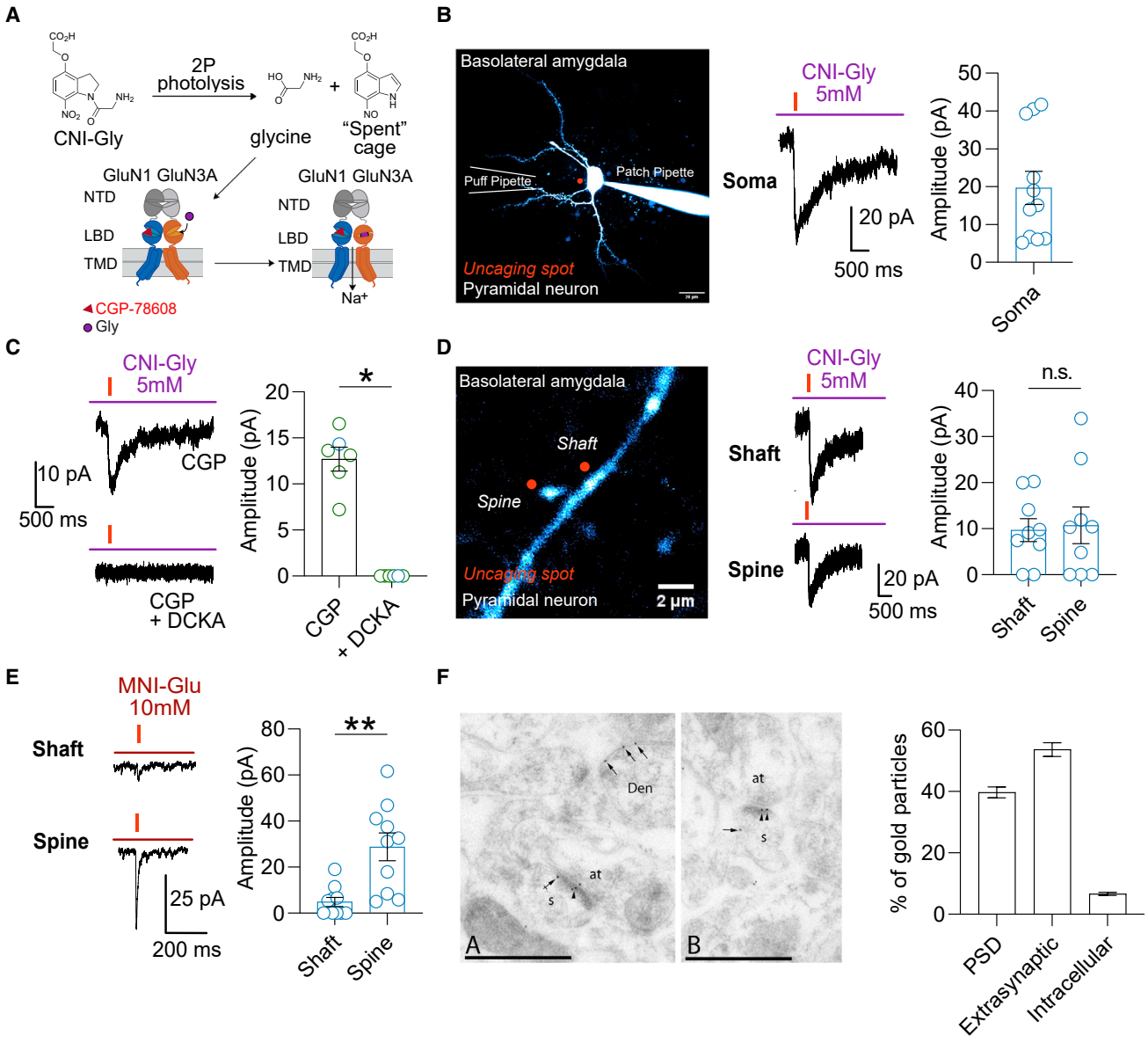

Figure 3. GluN1/GluN3A receptors are diffusively distributed across different neuronal subcellular compartments

(A) Scheme of uncaging reaction for CNI glycine (CNI-Gly) upon illumination and glycine action on GluN1/GluN3A receptors. Uncaging experiments were performed in the continuous presence of CGP-78608 (1 μM).

(B) Left: 2PLSM image of a fluorescently labeled BLA pyramidal neuron (PN). Right: example trace and summary plot of amplitudes of photolysis-evoked currents (obtained in the somas of BLA PNs) with a local application of 10 mM CNI-Gly (20-ms duration, n = 11).

(C) Photolysis-evoked currents are fully inhibited by DCKA (control versus DCKA, n = 6, p = 0.0313; Wilcoxon test). The plotted values represent data points obtained in both BLA PNs (blue) and S1 SST-INs (green).

(D) Amplitudes of light-evoked glycine currents in the shaft and spines of BLA PNs (n = 9, p = 0.8369, paired t test).

(E) Same as (D) but using MNI glutamate (MNI-Glu; 1-ms duration, n = 10, p = 0.0021, paired t test).

(F) Electron micrographs showing immunogold particles for the GluN3A subunits in the BLA. Den, dendritic shaft; s, dendritic spine; at, axon terminal. Arrowhead, postsynaptic density (PSD); crossed arrow, perisynaptic site; arrow, extrasynaptic site. Scale bars, 0.5 μm. Right: quantification of the subcellular distribution of GluN3A immunogold particles (PSD [39.7% ± 1.0%), extrasynaptic [53.7% ± 1.3%], and intracellular [6.6% ± 0.3%], n = 3).

(B–F) Bars indicate mean ± SEM.

in GluN3A KO slices, further confirming the requirement of GluN3A subunits (Figures 4A and 4B). A similar alteration in holding currents was obtained with the compound EU1180-438 (Zhu et al., 2020), a selective allosteric inhibitor of GluN1/GluN3A receptors (Figure S4A). Hence, excitatory glycine GluN1/GluN3A receptors can generate tonic inward currents in adult forebrain neurons. We obtained further evidence for the tonic activation of eGlyRs by exploiting their exquisite sensitivity to the redox

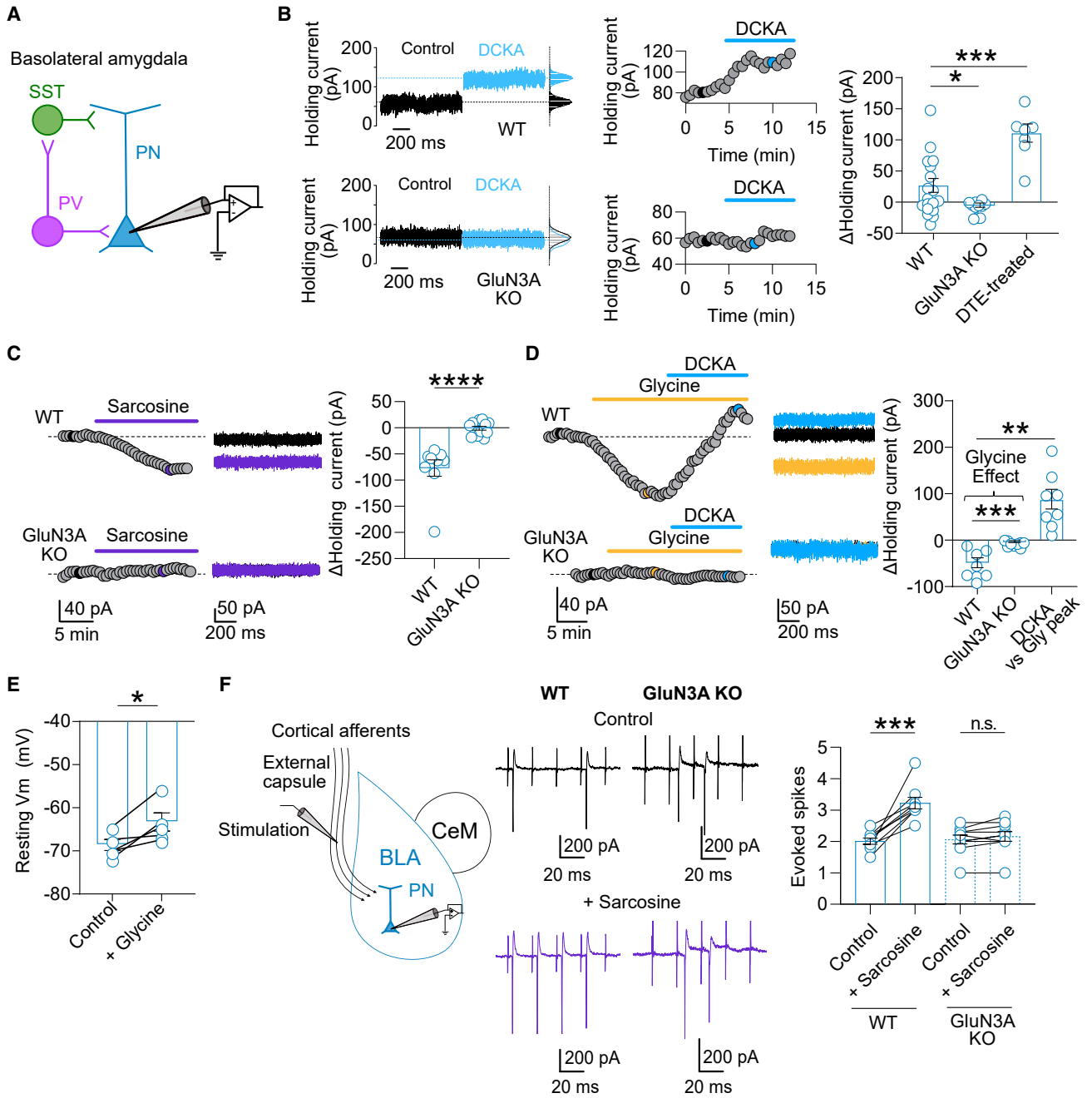

Figure 4. eGlyRs are tonically active and impact the neuronal excitability of BLA PNs

(A) Schematic representation of the canonical cellular organization of basolateral amygdala (BLA) microcircuit depicting a whole-cell patch-clamped pyramidal neuron (PN).

(B) Example traces, time course, and summary plot of the variations in the holding currents in BLA PNs upon DCKA (500 μM) application. Effect is shown for WT, GluN3A KO mice, and DTE-treated slices (WT [n = 18] versus GluN3A KO [n = 11], p = 0.0478; WT [n = 18] versus DTE-treated [n = 7], p = 0.0003, Kruskal-Wallis followed by Dunn's multiple comparisons test).

(C) Same as (B) but for the bath application of the glycine transporter GlyT1 inhibitor sarcosine (WT [n = 9] versus GluN3A KO [n = 13], unpaired t test).

(D) Bath application of glycine (10 μM) induced DCKA-sensitive inward currents in BLA PNs in the slices from WT but not GluN3A KO mice (WT [n = 8] versus GluN3A KO [n = 9], p = 0.0003, Mann-Whitney U test; WT [n = 8] versus DCKA [8], p = 0.0078, Wilcoxon test).

(E) Summary plot of resting membrane potential values for BLA PNs obtained in control conditions and after the bath application of glycine (10 μM; control [n = 5] versus glycine 10 μM [n = 5]; p = 0.0283, paired t test).

(legend continued on next page)

state. We previously showed that reducing agents profoundly enhance the glycine sensitivity of eGlyRs (Grand et al., 2018). Accordingly, the amplitude of eGlyR-mediated tonic currents in BLA PNs was significantly increased in 1,4-dithioerythritol (DTE)-treated slices (Figure 4B). These results suggest that in BLA PNs, GluN1/GluN3A receptors (at least a fraction) are in an oxidized state and that glycine levels around PNs are not sufficient to saturate eGlyRs. This conclusion was further buttressed by the observation that the application of CGP-78608, which reveals the occupancy of GluN1 glycine-binding sites, enhanced holding currents in DTE-treated but not in control slices (Figure S4B). We next wondered whether increasing extracellular glycine levels could also increase eGlyR tonic activity. Boosting extracellular glycine concentrations using the glycine transporter GlyT1 inhibitor sarcosine (50 μM) augmented tonic inward currents in BLA neurons, an effect absent in GluN3A KO slices (Figure 4C). Compatible with increased extracellular glycine levels, the occupancy of GluN1 glycine-binding sites was also significantly higher in the presence of sarcosine (Figure S4C). Moreover, direct bath application of glycine (10 μM) induced inward currents in BLA PNs that were completely blocked by DCKA and absent in the brain slices from GluN3A KO mice (Figure 4D). Altogether, these findings show that the eGlyRs in the PNs of the BLA are constitutively active and can signal possible variations in extracellular glycine concentrations.

Finally, we investigated the impact of eGlyR-mediated tonic currents on the resting membrane potential (Vm_{rest}) and excitability of BLA neurons. In agreement with the excitatory action of eGlyRs, the bath application of 10 μM glycine significantly depolarized BLA PNs (Figure 4E). In addition, using cell-attached recordings, we observed that the spiking activity induced by synaptic stimulation was markedly increased under sarcosine in control but not in GluN3A KO slices (Figure 4F), revealing the functional importance of GluN1/GluN3A-receptor-mediated currents in controlling BLA PN excitability. Overall, these results support the notion that eGlyRs act as sensors of extracellular glycine with direct influence on neuronal function in BLA circuits.

eGlyRs control S1 SST-IN resting membrane potential and excitability

SST-INs stand out from other interneurons like PV-INs by their high input resistance and more depolarized resting membrane potential (Pala and Petersen, 2015). Thus, we tested whether the tonic activation of GluN1/GluN3A receptors contributes to these distinctive features of SST-INs. Similar to BLA PNs, blocking eGlyRs' function with DCKA or EU1180-438 reduced the leak currents in S1 SST-INs (Figures 5A, 5B and S5A). To probe the functional impact of such tonic currents, we evaluated the effect of eGlyR recruitment on S1 SST-IN resting membrane potential. Pressure-applied glycine (1 mM, no. CGP-78608) in L2/3 of S1 depolarized SST-INs but not the other neuronal types tested (PV-INs, VIP-INs, and PNs) (Figure 5C). This selective excitatory action of glycine on S1 SST-INs was abolished in the brain slices from GluN3A KO mice, confirming the engagement of GluN1/GluN3A receptors (Figure 5C). In the current-clamp configuration, blocking tonic eGlyR activity through the application of DCKA, but not the Glu-binding site antagonist D-AP5, shifted the Vm_{rest} of S1 SST-INs to more hyperpolarized potentials (Figure 5D). No such effect of DCKA was observed on the neocortical PV-INs that lack the functional expression of GluN1/GluN3A receptors. Accordingly, the SST-INs from GluN3A KO mice displayed a more hyperpolarized Vm_{rest} than the SST-INs from control mice (Figure 5E). We further investigated the impact of eGlyR-mediated tonic currents on neuronal excitability by comparing the relationship between output firing and current injection in the S1 SST-INs from WT and GluN3A KO mice. The removal of GluN3A subunits induced a significant decrease in the excitability of SST-INs by increasing the current threshold for AP induction (Figure 5F; Table S1). These findings unveil an unsuspected role of GluN1/GluN3A receptors in setting S1 SST-IN Vm_{rest} and suggest that ambient extracellular glycine concentrations are a contributing factor to SST-INs excitability. To test this hypothesis directly, we incubated the slices with the enzyme glycine oxidase (GO), an approach known to reduce extracellular glycine levels efficiently and specifically (Ferreira et al., 2017; Le Bail et al., 2015; Papouin et al., 2012). Surprisingly, under these conditions, the Vm_{rest} of S1 SST-INs became even more depolarized and increased cell excitability (Figures 5G and 5H). However, the effect was still mediated by GluN3A-containing receptors, as GO incubation did not alter the Vm_{rest} of the S1 SST-INs from GluN3A KO slices (Figure 5G). Because of their atypical gating mechanism in which glycine acts both as an agonist (on GluN3A) and a functional antagonist (on GluN1), GluN1/GluN3A receptors display complex dependence on glycine concentrations, as manifested by bell-shaped dose-response curves (Awobuluyi et al., 2007; Chatterton et al., 2002; Madry et al., 2007). Accordingly, depending on the respective occupancy of the GluN1 and GluN3A binding sites, diminishing glycine concentrations can result in enhanced receptor activity. Therefore, we wondered whether such an effect could contribute to the apparent contradictory effects of GO on S1 SST-IN Vm_{rest}. We observed that the bath application of CGP-78608 increased the holding currents from S1 SST-INs, indicative of extracellular glycine levels sufficient to occupy (at least a fraction of) inhibitory GluN1 binding sites (Figure S5B). This effect was significantly reduced (but not abolished) in GO-incubated slices (Figure S5B), indicating that reduced glycine levels in the neocortex facilitate GluN1/GluN3A receptor activation by decreasing GluN1 subunit occupancy and subsequent receptor desensitization.

The clear influence of CGP-7806 on the holding currents of SST-INs in S1 contrasted with the lack of effect observed in BLA PNs (see Figure S4B). These results point to the differential occupancy of eGlyR agonist-binding sites under basal conditions between the two cell types. This effect could not be easily accounted for by the differences in the redox states of the

(F) Left: illustration of experimental approach used to probe the changes in the excitability of BLA PNs. Right: sarcosine enhances the action potential firing of BLA PNs in response to extracellular stimulation in WT but not in GluN3A KO mouse slices (WT: control versus sarcosine [n = 9], p = 0.0004; paired t test; GluN3A KO: control versus sarcosine [n = 10], p = 0.0957, paired t test).
(B–F) Bars indicate mean ± SEM.

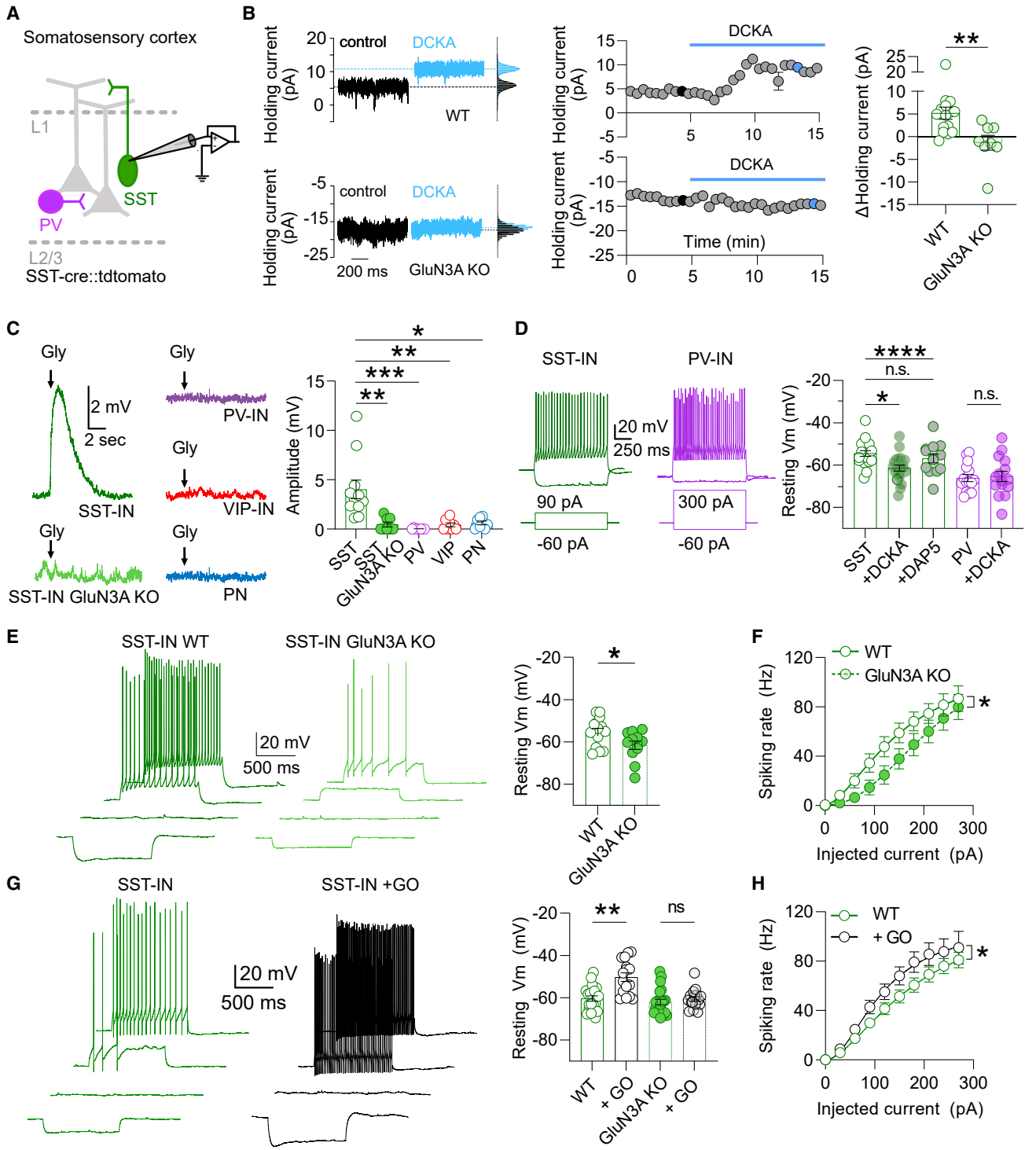

Figure 5. eGlyRs control the resting membrane potential of neocortical SST-INs

(A) Schematic representation of the canonical cellular organization of layer 2/3 in S1 depicting a whole-cell patch-clamped SST-IN.

(B) Example traces, time course, and summary plot of the variations in the holding currents in SST-INs upon DCKA (500 μM) application in WT and GluN3A KO mice (WT [n = 18] versus GluN3A KO [n = 11], p = 0.0478, Kruskal-Wallis followed by Dunn's multiple comparisons test).

(C) Example traces and summary plot of the measured EPSPs obtained in response to the puff application of glycine (1 mM) in different cell populations of layer 2/3 of S1. Note significantly larger membrane depolarizations in SST-INs and absence in GluN3A KO mice (SST-INs [n = 11] versus PNs [n = 8], p = 0.0203; versus

(legend continued on next page)

receptors, as the eGlyR currents in S1 SST-INs showed a marked sensitivity to the reducing agent DTE (Figure S5C) similarly to their BLA PN counterparts (see Figure S4B). We previously observed that the glycine transporter GlyT1 actively removes the glycine around BLA PNs (see Figure 4C). To further investigate the cellular mechanisms responsible for the differential occupancy of eGlyR glycine sites, we tested whether a similar effect was present in S1 SST-INs. In contrast to BLA PNs, inhibiting the glycine transporter GlyT1 with sarcosine had no effect on the holding currents recorded from S1 SST-INs (Figure S5D). A differential influence of sarcosine on holding currents was also observed when comparing, within the BLA, PNs and SST-INs that also express eGlyRs (Figure S4E). Overall, these results reveal that the occupancy of eGlyR glycine-binding sites under basal conditions differs across neuronal types, being higher in inhibitory neurons than in pyramidal cells, likely because of differential extracellular ambient glycine levels.

D-serine, while acting as a full co-agonist at GluN1/GluN2 receptors (Mothet et al., 2000), acts as a weak partial agonist at eGlyRs, thus inhibiting the eGlyR currents activated by glycine (Awobuluyi et al., 2007; Chatterton et al., 2002; Grand et al., 2018). Despite the observation that exogenous D-serine application inhibited both glycine-puff-evoked and holding currents in S1 SST-INs (Figures S5E and S5F), tonic eGlyR currents were not altered in the brain slices from serine racemase KO mice (Figures S4F and S5G). These findings indicate that extracellular glycine levels but not D-serine mainly control eGlyR activity.

In vivo function of eGlyRs modulates the activity of neocortical circuits

In order to evaluate the network relevance of eGlyRs, we tested how interfering with eGlyR the expression levels selectively in the SST-INs of the adult brain affects neuronal activity in S1. For this, we used an shRNA approach that effectively reduced the glycine-evoked currents in S1 SST-INs without any noticeable effect in the function of classical NMDARs (see STAR Methods; Figures 6A and S6A–S6E).

In the neocortex, SST-INs are known to efficiently control the activity of pyramidal cells (Gentet et al., 2012; Muñoz et al., 2017; Yaeger et al., 2019). We thus reasoned that the tonic activity of eGlyRs might impact the local cortical network dynamics through the modulation of SST-IN-mediated inhibition. To test this hypothesis, we first evaluated the impact of eGlyRs on the *in vivo* activity of SST-INs using multiphoton intravital calcium imaging from head-fixed mice free to run on a circular treadmill (Figures 6B and 6C). We observed that the reduced expression of GluN3A subunits in S1 SST-INs depressed the activity (expressed as fluorescence changes ΔF/F) of this neuronal population, especially during periods associated with locomotion, in agreement with the loss of eGlyR-mediated excitation (Figures 6C and 6D). In the neocortex, spontaneous activity is strongly related to the animal behavioral state (McGinley et al., 2015; Niell and Stryker, 2010; Poulet and Petersen, 2008; Reimer et al., 2014; Stringer et al., 2019a). Particularly, locomotion, which is often associated with the changes in arousal, has a profound effect on sensory responses (Dipoppa et al., 2018; Niell and Stryker, 2010). This important cortical computation is thought to arise from local interneuron interactions involving the activity of disinhibitory circuits containing VIP-INs and SST-INs (Dipoppa et al., 2018; Pakan et al., 2016). We, therefore, investigated the effect of downregulating the GluN3A levels in SST-INs on pyramidal cell activity (Figure 6E). *In vivo* 2P calcium fluorescence signals were measured during stationary periods as well as during the periods of locomotion that are known to depolarize PNs in mice (Dipoppa et al., 2018; McGinley et al., 2015; Pakan et al., 2016; Saleem et al., 2013). The selective expression of shGluN3A in S1 SST-INs led to an increase in PN activity during resting periods, a change compatible with the reduced inhibition of L2/3 PNs (Figures 6F and 6G). Moreover, in control mice, the periods of locomotion were associated with a higher cortical activity. This behavioral modulation of the cortical state was substantially reduced by interfering with the GluN3A expression in SST-INs, which led to a smaller locomotion modulation index (LMI; see STAR Methods) as well as a decrease in the correlation between PN activity and running speed (Figures 6G and 6H). In fact, pyramidal cell activation increased sharply with running speed, an effect eliminated following the expression of shGluN3A in SST-INs (Figure 6I). Similarly, the selective deletion of GluN1 subunits from S1 SST-INs to prevent the formation of eGlyRs strongly decreased the activity of S1 SST-INs (Figures 6J and 6K) and impaired the response of PNs to behavioral transitions from static to running periods (Figure 6L). Taken together, these results establish that neocortical eGlyRs are operational *in vivo*, being essential for the behavior-dependent function of cortical microcircuits through the targeted control of SST-IN excitability.

PV-INs [n = 8], $p < 0.0001$; versus VIP-INs [n = 8], $p = 0.0016$; SST-INs GluN3A KO [n = 8], $p = 0.0012$, Kruskal-Wallis followed by Dunn's multiple comparisons test).

(D) Left: representative current-clamp traces of membrane potential responses to injections of current steps applied to SST-INs (green) and PV-INs (fuchsia) in S1. Right: summary plot of the resting membrane potential values for SST-INs and PV-INs obtained in control conditions and after the addition of DCKA (500 μM) or D-AP5 (50 μM; SST versus SST + DCKA [n = 20], $p = 0.0256$; PV versus PV + DCKA [n = 15], $p > 0.9999$; control [n = 20] versus D-AP5 [n = 13], $p > 0.99$; Kruskal-Wallis followed by Dunn's multiple comparisons test).

(E) Same as (D) but for current-clamp recordings performed in the slices from WT and GluN3A KO mice. Left: electrophysiological traces represent the membrane potential responses to injections of current steps of increasing amplitude (−60, 0, 60, and 90 pA) to SST-INs. Right: SST-INs Vm_{rest} values are more hyperpolarized in GluN3A-lacking slices (WT [n = 14] versus GluN3A KO [n = 12], $p = 0.0356$, Mann-Whitney U test).

(F) Spiking frequency as a function of injected current for the SST-INs recorded in the slices from WT and GluN3A KO mice. Solid line represents the fit of Equation 1 (see STAR Methods) that is statistically different between WT [n = 14] and GluN3A KO [n = 12] mice; $p = 0.001$, extra-sum-of-squares F test.

(G) Same as (E) but for the current-clamp recordings performed in the slices treated with the enzyme glycine oxidase (GO). Reducing extracellular glycine levels with glycine oxidase depolarizes the Vm_{rest} values of SST-INs in the slices from WT but not GluN3A KO mice (WT [n = 20] versus WT + GO [n = 16], $p = 0.0012$; GluN3A KO [n = 21] versus GluN3A KO + GO [n = 16], $p = 0.6652$, Kruskal-Wallis followed by Dunn's multiple comparisons test).

(H) Same as (F) but for the brain slices incubated with glycine oxidase (WT [n = 18] versus GO [n = 11], $p = 0.001$, extra-sum-of-squares F test).

(B–G) Bars indicate mean ± SEM.

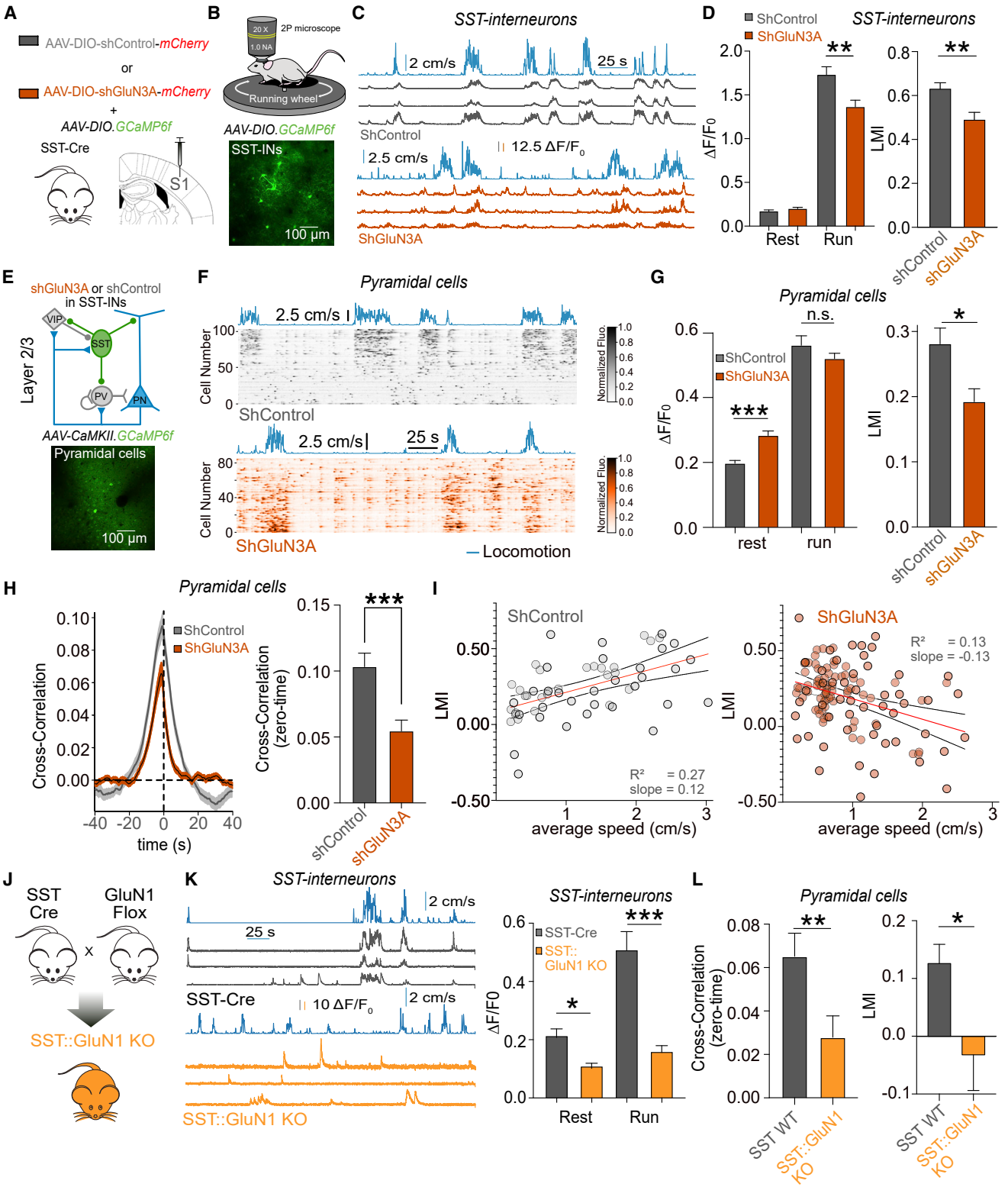

(legend on next page)

eGlyR activity is plastic and controls the stability of fear memories

In a final set of experiments, we explored the physiological relevance of eGlyR activity in the BLA. The amygdala plays an important role in controlling emotional and social behaviors and is intimately involved in the development of conditional fear (Gründemann and Lüthi, 2015; Johansen et al., 2011). We thus investigated whether exposing animals to a cued fear-conditioning protocol induces a change in eGlyR-mediated tonic currents, as observed *ex vivo* with the manipulation of extracellular glycine levels (Figure 4). After a single learning session (Figure 7A), animals were sacrificed and probed for the occupancy of eGlyR agonist-binding sites using CGP-78608-mediated enhancement of tonic currents from BLA PNs as a proxy. Under these experimental conditions, we observed clear potentiating effects by CGP-78608 that were essentially absent in naive animals (Figure 7B), evidencing the enhanced occupancy of eGlyR glycine sites. These results strikingly mirrored those obtained in the slices treated with the GlyT1 inhibitor sarcosine (see Figure S4C). Hence, stress stimuli can alter the tonic activity of eGlyRs in the BLA compatible with increased levels of extracellular glycine.

Dopamine innervation and release participate in the behavior-dependent modulation of BLA neuronal excitability (Johansen et al., 2011; Muller et al., 2009; Tang et al., 2020). Because dopamine can induce glycine release through the reverse transport of GlyT1 (Shibasaki et al., 2017), we tested whether the recruitment of dopaminergic signaling in the BLA could regulate eGlyR activity. In the slices treated with dopamine, but not in control ones, CGP-78608 enhanced the tonic currents of BLA PNs (Figure 7C), thus recapitulating the observation on fear-conditioned animals. Furthermore, in the dopamine-treated slices, DCKA application on BLA PNs revealed enhanced tonic GluN1/GluN3A-mediated currents, indicating increased eGlyR activity (Figure 7D). In agreement with increased levels of endogenous extracellular glycine levels, the effects of both sarcosine and exogenous glycine on holding currents were significantly reduced following dopamine action (Figures S7A and S7B). Altogether, these results show that the eGlyR tonic activity in the BLA is dynamically tuned by the animal behavior state as well as by dopaminergic signaling.

The activation of the classical Glu-binding NMDARs in the BLA is mandatory for the acquisition of Pavlovian cued fear conditioning and its extinction (Johansen et al., 2011). Contrasting with this critical role of conventional NMDARs in the acquisition of fear memories, the viral expression of shGluN3A constructs in BLA neurons (Figures 7E and S6F) had minimal impact on the expression of cued fear following tone-foot shock pairing protocols (Figure 7F), indicating that eGlyRs do not participate in the acquisition of fear memory. However, subsequent testing 24 h later revealed a blunted recall of fear memory, as evidenced by lower freezing levels to the first tones of the extinction protocol in shGluN3A-treated animals (Figure 7F). This diminished fear persisted throughout day 1, yet behavioral analysis of fear responses at the end of the fear extinction period (day 2) revealed a similar extinction rate and endpoint between shControl- and shGluN3A-treated animals (Figure 7F). Therefore, GluN1/GluN3A receptors appear to be involved in the stabilization of the fear memory but not in the acquisition and "de-acquisition" phases per se. Immunohistochemical analysis of AAV infections revealed a clear preference for shRNA expression for PNs versus INs, indicating that the observed behavior alterations are likely associated with the eGlyRs from BLA principal cells (Figure S7C). We also observed that basal anxiety and locomotion were minimally affected by eGlyR downregulation (Figure S7D). Overall,

Figure 6. *In vivo* activity of eGlyRs shapes the behavior-dependent modulation of neocortical networks

(A) Schematic illustration of the experimental conditions used to monitor the impact of eGlyRs on cortical activity (see STAR Methods).

(B) 2P calcium imaging in S1 of awake mice. Mice were head fixed and were free to run on a circular treadmill. Bottom: *in vivo* 2PSLM images of S1 SST-INs labeled with GCaMP6s.

(C) Example traces of GCaMP6s fluorescence transients ($\Delta F/F_0$) obtained from the individual S1 SST-INs in the SST-Cre mice expressing either shControl (top, gray traces) or shGluN3A (bottom, orange traces) with corresponding locomotion trace (cm/s, blue traces).

(D) Changes in GCaMP6s fluorescence quantified as average $\Delta F/F_0$ in SST-INs during rest and run states in SST-Cre mice expressed with shControl or shGluN3A (rest: shControl [n = 447] versus shGluN3A [n = 385 neurons], p = 0.1562; run: shControl [n = 447] versus shGluN3A [n = 385 neurons], p = 0.0048, Mann-Whitney test). Right: histogram of the distribution of locomotion modulation index (LMI, p = 0.012, Mann-Whitney test).

(E) Top: schematic illustration of layer 2/3 microcircuits in S1; bottom: *in vivo* 2PSLM images of S1 PNs labeled with GCaMP6f.

(F) Raster plot of the pyramidal cell activity in the S1 from awake mice spontaneously transitioning between resting periods and periods of locomotion. SST-Cre mice expressed shGluN3A of shControl sequences in SST-INs. Each row represents a neuron sorted by weight on the first principal component (PC) of their activity.

(G) Same as (D) but for L2/3 PNs (rest: shControl [n = 73 sessions, 5,773 neurons] versus shGluN3A [n = 120 sessions, 6,517 neurons], p < 0.001; run: shControl [n = 73] versus shGluN3A [n = 120], p = 0.7394). Right: LMI (p = 0.0217, Mann-Whitney test).

(H) Left: cross-correlation between $\Delta F/F_0$ and running speed (left) for the PNs in the mice expressing shControl of shGluN3A in SST-INs. Thick lines represent average (shControl [n = 73 sessions, 5,773 neurons] and shGluN3A [n = 120 sessions, 6,517 neurons]) and SEM. Right: summary plot of cross-correlation values at zero time for the experiments listed on the left panel.

(I) Variation in LMI with the average running speed for L2/3 PNs. Red lines are linear fits through all points with gray lines representing 95% confidence intervals of the fits. A positive significant correlation was obtained for shControl, whereas a negative correlation was observed for shGluN3A (shControl: p < 0.001, R^2 = 0.27, n = 73; shGluN3A: p < 0.001, R^2 = 0.13, n = 120).

(J) Genetic deletion of the GluN1 subunits from SST-INs by crossing SST-Cre mice with mice carrying a floxed GluN1 gene.

(K) Same as (C) and (D) but for the SST-INs from WT or SST:GluN1 KO mice (rest: WT [n = 120 neurons] versus SST:GluN1 KO [n = 220 neurons], p = 0.0005; run: WT [n = 120 neurons] versus SST:GluN1 KO [n = 220 neurons], p < 0.0001, Mann-Whitney test).

(L) Effect of the deletion of GluN1 subunit from SST-INs on the cross-correlation between $\Delta F/F_0$ and running speed as well as the locomotion modulation index of PNs in S1 (WT [n = 40 sessions, 1,141 neurons] versus SST:GluN1 KO [n = 47 sessions, 1,322 neurons], cross-correlation, p = 0.0021; LMI, p = 0.0436, Mann-Whitney test).

(D, G, H, K and L) Bars indicate mean ± SEM.

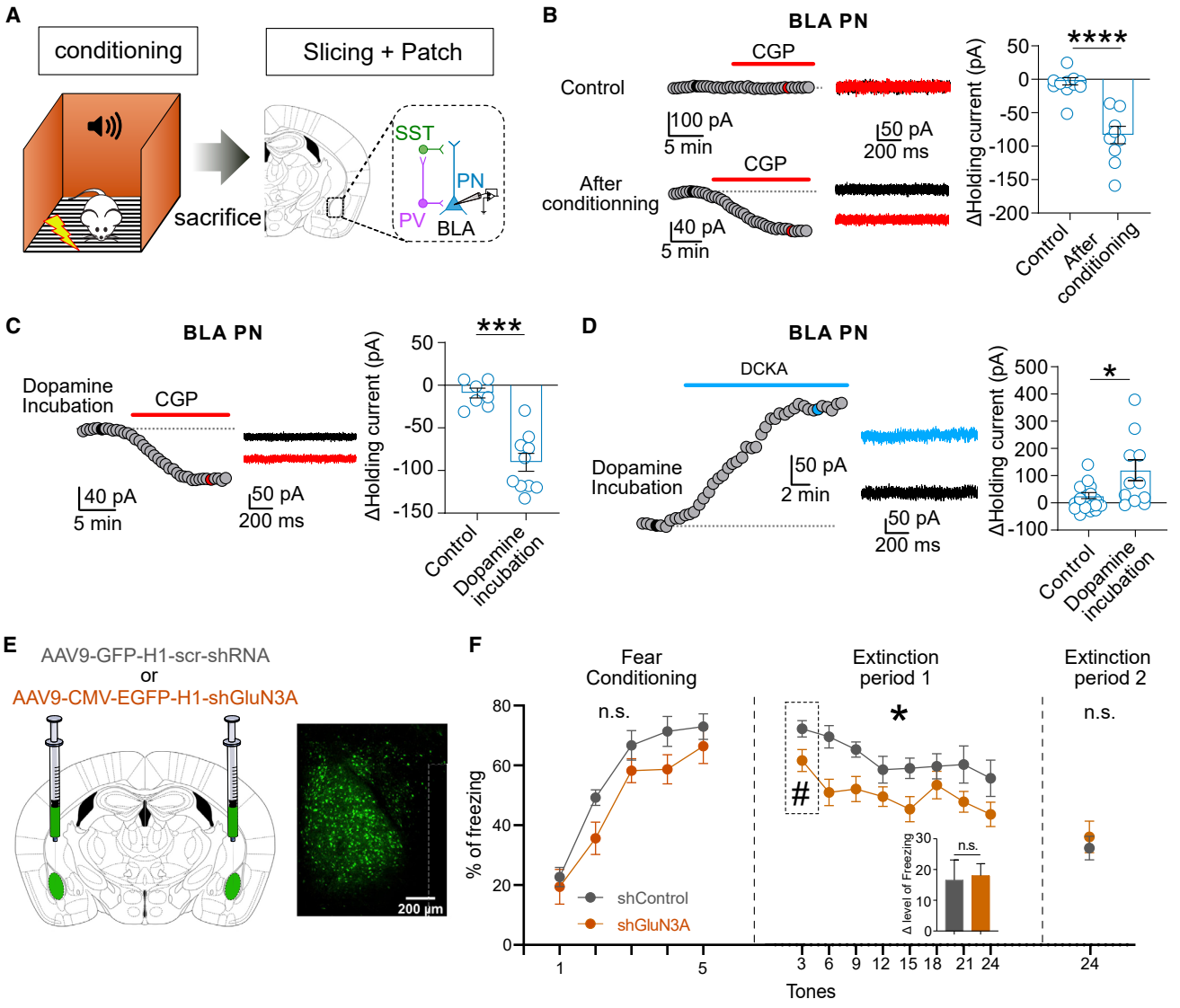

Figure 7. eGlyR activity is plastic and participate in the consolidation of fear memories

(A) Schematic of the experimental approach used in (B). Mice were exposed to a fear-conditioning protocol (see STAR Methods) and then quickly sacrificed for brain slicing and patch-clamp experiments on BLA PNs.

(B) CGP-78608 (1 μM) enhances the holding currents of the BLA PNs from the mice subjected to the fear-conditioning protocol but not in control animals (control [n = 11] versus after conditioning [n = 9], $p < 0.0001$, Mann-Whitney U test).

(C) Similar to (B), but for the slices incubated with dopamine (60 μM). Note that prior exposure to dopamine enhanced the holding currents of BLA PNs induced by CGP-78608 (1 μM) when compared with control (non-incubated) slices (control [n = 7] versus dopamine incubation [n = 10], $p = 0.0002$, Mann-Whitney U test).

(D) DCKA application revealed enhanced tonic inward currents in BLA PNs after dopamine incubation (control [n = 18] versus dopamine incubation [n = 11], $p = 0.0108$, Mann-Whitney U test).

(E) Cartoon depicting the locations used for bilateral viral injections in BLA neurons. Mice were injected with either AAV9-GFP-H1-scr-shRNA (shControl) or AAV9-CMV-EGFP-H1-shGluN3A (shGluN3A). Inset shows infected BLA PNs expressing the green reporter (GFP or EGFP).

(F) Effect of expressing shControl (n = 10 animals) or shGluN3A (n = 11 animals) in BLA neurons on the acquisition, consolidation, and extinction of conditioned fear. Fear conditioning—interaction: $F(4,76) = 0.7496$, $p = 0.5613$ and group difference: $F(1,19) = 0.1723$, $p = 0.6827$; extinction period 1—interaction: $F(7,133) = 0.9124$, $p = 0.4990$ and group difference: $F(1,19) = 6.202$, *$p = 0.0222$, two-way repeated measures ANOVA. Freezing during the first 3 tones #, $p = 0.0357$, Mann-Whitney test. Rate of fear extinction during period 1—inset, $p = 0.6539$, Mann-Whitney test. Both groups reached similar extinction levels by the end of day 2. (B, C, D, and F) Bars indicate mean ± SEM.

these results point to the involvement of BLA eGlyRs in a specific period of fear learning, corresponding to the retention phase wherein newly acquired fear memories are stabilized and consolidated before their retrieval or extinction.

DISCUSSION

Our combined results in amygdalar and neocortical circuits reveal GluN3A-containing eGlyRs as an overlooked signaling

system with biologically relevant and widespread actions in the adult brain. We show that adult GluN3A is expressed in distinct neuronal populations and brain areas and assembles mainly as excitatory GluN1/GluN3A receptors that sense ambient glycine and play important functional roles. The cell specificity of eGlyR expression is brain region dependent. In the neocortex, functional GluN1/GluN3A receptors are detected at a high level only in SST-INs, with no or very little expression in all the other cell types tested (PNs, PV-INs, and VIP-INs). By contrast, in the BLA, functional eGlyRs are detected in a greater diversity of neuronal types, including not only PNs and SST-INs but also PV-INs.

Despite the recent evidence that GluN1 and GluN3A subunits can form functional receptors in the adult brain (Otsu et al., 2019), the endogenous mechanisms controlling the activation of such receptors were still mostly unknown. We have now revealed that eGlyRs are directly gated by the endogenous glycine that is present in the extracellular milieu generating tonic excitatory currents that participate in setting resting membrane potential and controlling neuronal excitability. Forebrain regions, such as the BLA and neocortex, receive little to no glycinergic innervation (Zeilhofer et al., 2005), suggesting that eGlyRs, at least in these brain areas, are unlikely to be activated by synaptic glycine transients. Investigation of the subcellular distribution of eGlyRs using 2P glycine uncaging revealed that GluN1/GluN3A receptors do not cluster at dendritic spines but rather diffusively distribute on the neuronal cell surface. Thus, our results are compatible with the hypothesis that eGlyRs are specialized in the detection of low ambient extracellular glycine concentrations, a property conferred by the high-affinity glycine-binding subunit GluN3A. The atypical gating of eGlyRs, where glycine binding to GluN3A triggers receptor opening, whereas the occupancy of GluN1 glycine sites induces desensitization, might work as an embedded auto-inactivation mechanism when ambient glycine concentrations surge to protect neurons from overexcitation. Glycine-activated GluN1/GluN3A receptors are also inhibited by D-serine. However, the results we obtained when using brain slices from animals lacking serine racemase suggest no clear effect of D-serine on tonic eGlyR activity. Future work is needed to better define the role of endogenous D-serine in modulating the function of eGlyRs.

We also established that the tonic eGlyR activity in the PNs of the BLA was modified by briefly exposing animals to a stress stimulus or by the activation of dopaminergic signaling. These findings highlight that GluN1/GluN3A-mediated signaling can be adjusted by the behavioral state and/or by the action of neuromodulators to control neuronal excitability. Our intravital calcium imaging data together with the behavioral analysis of fear conditioning also indicate that eGlyRs are functional and operational *in vivo*. By defining the operating principles of this new class of neurotransmitter receptors and their ability with regard to state-dependent regulation, our work provides the necessary mechanistic framework for advancing our understanding of unconventional NMDAR function in the CNS.

The use of CGP-78608 as a blocker of eGlyR desensitization (Grand et al., 2018) allowed us to have quantitative insights into the variation in extracellular glycine levels across brain regions. Our results unveiled that the amount of desensitized eGlyRs is greater in SST-INs (both S1 and BLA) than in BLA PNs and that this difference is likely to originate from the variability in extracellular glycine levels. Blocking the function of the glycine transporter GlyT1 resulted in the development of eGlyR-mediated inward currents in BLA PNs, compatible with glycine accumulation in the extracellular space, but minimally altered the holding currents in SST-INs (both BLA and S1). This differential effect suggests that dissimilar density/function of GlyT1 around inhibitory and excitatory neurons, with its ability to control extracellular glycine levels (Harvey and Yee, 2013), is a probable contributing factor. Our observation that eGlyR glycine sites are not saturated and differentially occupied also suggests that extracellular glycine levels and, consequently, the activation of eGlyRs can be subject to physiological regulation. In BLA PNs, dopamine exposure increased the occupancy of GluN1 glycine-binding sites (indexed by CGP-78608) as well as the magnitude of eGlyR tonic currents (revealed by DCKA). Decreased effect of sarcosine on holding currents after dopamine receptor activation suggests the modulation of GlyT1 function and increased availability of extracellular glycine in dopamine-treated slices. This increase in glycine leads to increased occupancy of both (activating) GluN3A and (inhibiting) GluN1 sites, with an overall net effect in favor of enhanced eGlyR activation. However, we cannot exclude the contribution of the changes in receptor properties (e.g., affinity of glycine sites). The regulation of eGlyR activity and responsiveness to the changes in extracellular glycine is a complex function due to the opposite yet overlapping influence of GluN1 and GluN3A agonist-binding sites on receptor gating. Generally, the present findings on eGlyR regulation call for a better understanding of how the regional and temporal variations in endogenous glycine levels are controlled in the extracellular environment of the CNS.

Contrasting with the ubiquitous presence of GluN1/GluN2 NMDARs in individual CNS neurons, eGlyRs display a restricted distribution limited to defined brain territories and neuronal cell types. Moreover, whereas classical NMDARs are enriched at synapses, respond to phasic Glu release, and require membrane depolarization to unblock Mg^{2+}, eGlyRs are mostly extrasynaptic, gated by glycine but insensitive to Glu and Mg^{2+}, and operate under a tonic regime at resting membrane potential. Drugs targeting conventional NMDARs often suffer from poor side effect profiles, including psychotogenicity (Javitt and Zukin, 1991; Lodge and Mercier, 2015). The widespread yet patchy (at both regional and cell levels) expression pattern of eGlyRs might represent an advantage for possible future GluN3A-targeted therapies regarding tolerability. GluN3A subunits are expressed in the human brain (Hodge et al., 2019), and alterations in the *Grin3a* gene have been associated with several neurological and psychiatric disorders, including schizophrenia, bipolar disorder, and epilepsy (Crawley et al., 2022; Mueller and Meador-Woodruff, 2004; Pfisterer et al., 2020). Our finding that GluN3A subunits are associated with the operational eGlyRs in the adult brain raises new perspectives in the signaling mechanisms by which this subunit participates in neuropathology. It also foregrounds eGlyRs as promising new targets for neuroactive compounds that may escape the psychotomimetic effects associated with classical NMDAR drugs.

STAR★METHODS

Detailed methods are provided in the online version of this paper and include the following:

- KEY RESOURCES TABLE
- RESOURCE AVAILABILITY
  - Lead contact
  - Materials availability
  - Data and code availability
- EXPERIMENTAL MODEL AND SUBJECT DETAILS
  - Mice
- METHOD DETAILS
  - Slice preparation
  - *Ex vivo* electrophysiology
  - Synthesis of CNI-Glycine (CNI-Gly)
  - Uncaging Experiments
  - Fluorescence *in situ* hybridization (FISH)
  - Immunoelectron microscopy
  - Viral injections
  - *In vivo* two-photon calcium imaging
  - Behavioral experiments
  - Anxiety tests
  - Pavlovian fear conditioning and extinction
  - Drugs and enzyme
- QUANTIFICATION AND STATISTICAL ANALYSIS
  - Analysis of *ex vivo* electrophysiological recordings
  - Two-photon data analysis
  - Confocal imaging data acquisition and analysis
  - Statistical analysis

SUPPLEMENTAL INFORMATION

Supplemental information can be found online at https://doi.org/10.1016/j.neuron.2022.05.016.

ACKNOWLEDGMENTS

We thank Nobuki Nakanishi and Stuart Lipton (Scintillon Institute, San Diego, USA) for providing the GluN3A KO mouse line, Peter Seeburg (University of Heidelberg, Germany) for providing the GluN1 Flox (NR1-2lox) mouse line, Darrick Balu (Harvard Medical School, USA) for the serine racemase KO mouse line, and Beatriz Rico (King's College, London, UK) for the initial AAV-DIO-shGluN3A constructs. This work was supported by the Agence Nationale de la Recherche (grants ANR-10-LABX-54 MEMOLIFE and ANR-11-IDEX-0001-02 to IBENS/P.P., ANR-GluBrain3A to P.P., and ANR-EXCIGLY to P.P. and N.R.), the European Research Council (ERC Advanced Grant #693021 to P.P. and ERC Starting Grant #678250 to N.R.), the Brain & Behavior Research Foundation (NARSAD young investigator grant #27653 to N.R.), and the US National Institutes of Health (GM053395 and NS111600 to G.C.R.E.-D.). We would also like to thank the Paris Brain Institute core facilities, namely iVector and ICMice phenopark.

AUTHOR CONTRIBUTIONS

S.B., D.D., M.C., P.P., and N.R. were involved in conceptualization. S.B. and D.D. performed slice electrophysiology and two-photon uncaging experiments. G.C.R.E.-D. designed and characterized CNI glycine. M.d.B.V.V. performed *in vivo* two-photon calcium imaging. A.M and I.P.-O. performed fluorescence *in situ* hybridization and contributed to AAV constructs. J.F., S.B., and D.P. performed behavioral tests. A.B. and J.L. designed and performed *in vivo* experiments using SST::GluN1 KO animals. R.L. performed electron microscopy. P.P. and N.R. wrote the manuscript, which was edited by all the authors. P.P. and N.R. were involved in supervision.

DECLARATION OF INTERESTS

The authors declare no competing interests.

Received: September 16, 2021
Revised: April 5, 2022
Accepted: May 13, 2022
Published: June 13, 2022

REFERENCES

Al-Hallaq, R.A., Jarabek, B.R., Fu, Z., Vicini, S., Wolfe, B.B., and Yasuda, R.P. (2002). Association of NR3A with the *N*-methyl-D-aspartate receptor NR1 and NR2 subunits. Mol. Pharmacol. *62*, 1119–1127. https://doi.org/10.1124/mol.62.5.1119.

Awobuluyi, M., Yang, J., Ye, Y., Chatterton, J.E., Godzik, A., Lipton, S.A., and Zhang, D. (2007). Subunit-specific roles of glycine-binding domains in activation of NR1/NR3 *N*-methyl-D-aspartate receptors. Mol. Pharmacol. *71*, 112–122. https://doi.org/10.1124/mol.106.030700.

Basu, A.C., Tsai, G.E., Ma, C.-L., Ehmsen, J.T., Mustafa, A.K., Han, L., Jiang, Z.I., Benneyworth, M.A., Froimowitz, M.P., Lange, N., et al. (2009). Targeted disruption of serine racemase affects glutamatergic neurotransmission and behavior. Mol. Psychiatry *14*, 719–727. https://doi.org/10.1038/mp.2008.130.

Chatterton, J.E., Awobuluyi, M., Premkumar, L.S., Takahashi, H., Talantova, M., Shin, Y., Cui, J., Tu, S., Sevarino, K.A., Nakanishi, N., et al. (2002). Excitatory glycine receptors containing the NR3 family of NMDA receptor subunits. Nature *415*, 793–798. https://doi.org/10.1038/nature715.

Ciabarra, M., Sevarino, A., Gahn, G., Pecht, G., Heinemann, S., and Sevarino, K.A. (1995). Cloning and characterization of chi-1: a developmentally regulated member of a novel class of the ionotropic glutamate receptor family. J Neurosci *15*, 6498–6508. https://doi.org/10.1523/JNEUROSCI.15-10-06498.1995.

Corrie, J.E.T., Kaplan, J.H., Forbush, B., Ogden, D.C., and Trentham, D.R. (2016). Photolysis quantum yield measurements in the near-UV; a critical analysis of 1-(2-nitrophenyl)ethyl photochemistry. Photochem. Photobiol. Sci. *15*, 604–608. https://doi.org/10.1039/C5PP00440C.

Crawley, O., Conde-Dusman, M.J., and Pérez-Otaño, I. (2022). GluN3A NMDA receptor subunits: more enigmatic than ever? J. Physiol. *600*, 261–276. https://doi.org/10.1113/JP280879.

Das, S., Sasaki, Y.F., Rothe, T., Premkumar, L.S., Takasu, M., Crandall, J.E., Dikkes, P., Conner, D.A., Rayudu, P.V., Cheung, W., et al. (1998). Increased NMDA current and spine density in mice lacking the NMDA receptor subunit NR3A. Nature *393*, 377–381. https://doi.org/10.1038/30748.

Dipoppa, M., Ranson, A., Krumin, M., Pachitariu, M., Carandini, M., and Harris, K.D. (2018). Vision and locomotion shape the interactions between neuron types in mouse visual cortex. Neuron *98*, 602–615.e8. https://doi.org/10.1016/j.neuron.2018.03.037.

Ellis-Davies, G.C.R. (2011). A practical guide to the synthesis of dinitroindolinyl-caged neurotransmitters. Nat. Protoc. *6*, 314–326. https://doi.org/10.1038/nprot.2010.193.

Favuzzi, E., Deogracias, R., Marques-Smith, A., Maeso, P., Jezequel, J., Exposito-Alonso, D., Balia, M., Kroon, T., Hinojosa, A.J., Maraver, E.F., and Rico, B. (2019). Distinct molecular programs regulate synapse specificity in cortical inhibitory circuits. Science *363*, 413–417. https://doi.org/10.1126/science.aau8977.

Ferreira, J.S., Papouin, T., Ladépêche, L., Yao, A., Langlais, V.C., Bouchet, D., Dulong, J., Mothet, J.P., Sacchi, S., Pollegioni, L., et al. (2017). Co-agonists differentially tune GluN2B-NMDA receptor trafficking at hippocampal synapses. eLife *6*, e25492. https://doi.org/10.7554/eLife.25492.

Gentet, L.J., Kremer, Y., Taniguchi, H., Huang, Z.J., Staiger, J.F., and Petersen, C.C.H. (2012). Unique functional properties of somatostatin-expressing GABAergic neurons in mouse barrel cortex. Nat. Neurosci. *15*, 607–612. https://doi.org/10.1038/nn.3051.

Grand, T., Abi Gerges, S., David, M., Diana, M.A., and Paoletti, P. (2018). Unmasking GluN1/GluN3A excitatory glycine NMDA receptors. Nat. Commun. *9*, 4769. https://doi.org/10.1038/s41467-018-07236-4.

Gründemann, J., and Lüthi, A. (2015). Ensemble coding in amygdala circuits for associative learning. Curr. Opin. Neurobiol. *35*, 200–206. https://doi.org/10.1016/j.conb.2015.10.005.

Harvey, R.J., and Yee, B.K. (2013). Glycine transporters as novel therapeutic targets in schizophrenia, alcohol dependence and pain. Nat. Rev. Drug Discov. *12*, 866–885. https://doi.org/10.1038/nrd3893.

Hodge, R.D., Bakken, T.E., Miller, J.A., Smith, K.A., Barkan, E.R., Graybuck, L.T., Close, J.L., Long, B., Johansen, N., Penn, O., et al. (2019). Conserved cell types with divergent features in human versus mouse cortex. Nature *573*, 61–68. https://doi.org/10.1038/s41586-019-1506-7.

Javitt, D.C., and Zukin, S.R. (1991). Recent advances in the phencyclidine model of schizophrenia. Am. J. Psychiatry *148*, 1301–1308. https://doi.org/10.1176/ajp.148.10.1301.

Johansen, J.P., Cain, C.K., Ostroff, L.E., and LeDoux, J.E. (2011). Molecular mechanisms of fear learning and memory. Cell *147*, 509–524. https://doi.org/10.1016/j.cell.2011.10.009.

Johnson, J.W., and Ascher, P. (1987). Glycine potentiates the NMDA response in cultured mouse brain neurons. Nature *325*, 529–531. https://doi.org/10.1038/325529a0.

Kleckner, N.W., and Dingledine, R. (1988). Requirement for glycine in activation of NMDA-receptors expressed in *Xenopus* oocytes. Science *241*, 835–837. https://doi.org/10.1126/science.2841759.

Le Bail, M., Martineau, M., Sacchi, S., Yatsenko, N., Radzishevsky, I., Conrod, S., Ait Ouares, K., Wolosker, H., Pollegioni, L., Billard, J.-M., and Mothet, J.P. (2015). Identity of the NMDA receptor coagonist is synapse specific and developmentally regulated in the hippocampus. Proc. Natl. Acad. Sci. USA *112*, E204–E213. https://doi.org/10.1073/pnas.1416668112.

Legendre, P (2001). The glycinergic inhibitory synapse. Cellular and Molecular Life Sciences CMLS. https://doi.org/10.1007/PL00000899.

Lodge, D., and Mercier, M.S. (2015). Ketamine and phencyclidine: the good, the bad and the unexpected. Br. J. Pharmacol. *172*, 4254–4276. https://doi.org/10.1111/bph.13222.

Madry, C., Mesic, I., Bartholomäus, I., Nicke, A., Betz, H., and Laube, B. (2007). Principal role of NR3 subunits in NR1/NR3 excitatory glycine receptor function. Biochem. Biophys. Res. Commun. *354*, 102–108. https://doi.org/10.1016/j.bbrc.2006.12.153.

Marco, S., Giralt, A., Petrovic, M.M., Pouladi, M.A., Martínez-Turrillas, R., Martínez-Hernández, J., Kaltenbach, L.S., Torres-Peraza, J., Graham, R.K., Watanabe, M., et al. (2013). Suppressing aberrant GluN3A expression rescues synaptic and behavioral impairments in Huntington's disease models. Nat. Med. *19*, 1030–1038. https://doi.org/10.1038/nm.3246.

Marco, S., Murillo, A., and Pérez-Otaño, I. (2018). RNAi-based GluN3A silencing prevents and reverses disease phenotypes induced by mutant huntingtin. Mol. Ther. *26*, 1965–1972. https://doi.org/10.1016/j.ymthe.2018.05.013.

Matsuzaki, M., Hayama, T., Kasai, H., and Ellis-Davies, G.C.R. (2010). Two-photon uncaging of γ-aminobutyric acid in intact brain tissue. Nat. Chem. Biol. *6*, 255–257. https://doi.org/10.1038/nchembio.321.

Matsuzaki, M., Honkura, N., Ellis-Davies, G.C.R., and Kasai, H. (2004). Structural basis of long-term potentiation in single dendritic spines. Nature *429*, 761–766. https://doi.org/10.1038/nature02617.

McGinley, M.J., Vinck, M., Reimer, J., Batista-Brito, R., Zagha, E., Cadwell, C.R., Tolias, A.S., Cardin, J.A., and McCormick, D.A. (2015). Waking state: rapid variations modulate neural and behavioral responses. Neuron *87*, 1143–1161. https://doi.org/10.1016/j.neuron.2015.09.012.

Mothet, J.P., Parent, A.T., Wolosker, H., Brady, R.O., Linden, D.J., Ferris, C.D., Rogawski, M.A., and Snyder, S.H. (2000). D-serine is an endogenous ligand for the glycine site of the *N*-methyl-D-aspartate receptor. Proc. Natl. Acad. Sci. USA *97*, 4926–4931. https://doi.org/10.1073/pnas.97.9.4926.

Mueller, H.T., and Meador-Woodruff, J.H. (2004). NR3A NMDA receptor subunit mRNA expression in schizophrenia, depression and bipolar disorder. Schizophr. Res. *71*, 361–370. https://doi.org/10.1016/j.schres.2004.02.016.

Muller, J.F., Mascagni, F., and McDonald, A.J. (2009). Dopaminergic innervation of pyramidal cells in the rat basolateral amygdala. Brain Struct. Funct. *213*, 275–288. https://doi.org/10.1007/s00429-008-0196-y.

Muñoz, W., Tremblay, R., Levenstein, D., and Rudy, B. (2017). Layer-specific modulation of neocortical dendritic inhibition during active wakefulness. Science *355*, 954–959. https://doi.org/10.1126/science.aag2599.

Murillo, A., Navarro, A.I., Puelles, E., Zhang, Y., Petros, T.J., and Pérez-Otaño, I. (2021). Temporal dynamics and neuronal specificity of Grin3a expression in the mouse forebrain. Cereb. Cortex *31*, 1914–1926. https://doi.org/10.1093/cercor/bhaa330.

Nicoll, R.A. (2017). A Brief History of Long-Term Potentiation. Neuron *93*, 281–290.

Niell, C.M., and Stryker, M.P. (2010). Modulation of visual responses by behavioral state in mouse visual cortex. Neuron *65*, 472–479. https://doi.org/10.1016/j.neuron.2010.01.033.

Niewoehner, B., Single, F.N., Hvalby, Ø., Jensen, V., Meyer zum Alten Borgloh, S., Seeburg, P.H., Rawlins, J.N.P., Sprengel, R., and Bannerman, D.M. (2007). Impaired spatial working memory but spared spatial reference memory following functional loss of NMDA receptors in the dentate gyrus. Eur. J. Neurosci. *25*, 837–846. https://doi.org/10.1111/j.1460-9568.2007.05312.x.

Oh, S.W., Harris, J.A., Ng, L., Winslow, B., Cain, N., Mihalas, S., Wang, Q., Lau, C., Kuan, L., Henry, A.M., et al. (2014). A mesoscale connectome of the mouse brain. Nature *508*, 207–214. https://doi.org/10.1038/nature13186.

Otsu, Y., Darcq, E., Pietrajtis, K., Mátyás, F., Schwartz, E., Bessaih, T., Abi Gerges, S., Rousseau, C.V., Grand, T., Dieudonné, S., et al. (2019). Control of aversion by glycine-gated GluN1/GluN3A NMDA receptors in the adult medial habenula. Science *366*, 250–254. https://doi.org/10.1126/science.aax1522.

Pachitariu, M., Stringer, C., Dipoppa, M., Schröder, S., Rossi, L.F., Dalgleish, H., Carandini, M., and Harris, K.D. (2017). Suite2p: beyond 10,000 neurons with standard two-photon microscopy. Preprint at bioRxiv. https://doi.org/10.1101/061507.

Pakan, J.M., Lowe, S.C., Dylda, E., Keemink, S.W., Currie, S.P., Coutts, C.A., and Rochefort, N.L. (2016). Behavioral-state modulation of inhibition is context-dependent and cell type specific in mouse visual cortex. eLife *5*, e14985. https://doi.org/10.7554/eLife.14985.

Pala, A., and Petersen, C.C.H. (2015). In vivo measurement of cell-type-specific synaptic connectivity and synaptic transmission in layer 2/3 mouse barrel cortex. Neuron *85*, 68–75. https://doi.org/10.1016/j.neuron.2014.11.025.

Paoletti, P., Bellone, C., and Zhou, Q. (2013). NMDA receptor subunit diversity: impact on receptor properties, synaptic plasticity and disease. Nat. Rev. Neurosci. *14*, 383–400. https://doi.org/10.1038/nrn3504.

Papageorgiou, G., and Corrie, J.E.T. (2000). Effects of aromatic substituents on the photocleavage of 1-acyl-7-nitroindolines. Tetrahedron *56*, 8197–8205. https://doi.org/10.1016/S0040-4020(00)00745-6.

Papouin, T., Ladépêche, L., Ruel, J., Sacchi, S., Labasque, M., Hanini, M., Groc, L., Pollegioni, L., Mothet, J.P., and Oliet, S.H.R. (2012). Synaptic and extrasynaptic NMDA receptors are gated by different endogenous coagonists. Cell *150*, 633–646. https://doi.org/10.1016/j.cell.2012.06.029.

Paul, A., Crow, M., Raudales, R., He, M., Gillis, J., and Huang, Z.J. (2017). Transcriptional architecture of synaptic communication delineates GABAergic neuron identity. Cell *171*, 522–539.e20. https://doi.org/10.1016/j.cell.2017.08.032.

Pérez-Otaño, I., Larsen, R.S., and Wesseling, J.F. (2016). Emerging roles of GluN3-containing NMDA receptors in the CNS. Nat. Rev. Neurosci. *17*, 623–635. https://doi.org/10.1038/nrn.2016.92.

Pérez-Otaño, I., Luján, R., Tavalin, S.J., Plomann, M., Modregger, J., Liu, X.-B., Jones, E.G., Heinemann, S.F., Lo, D.C., and Ehlers, M.D. (2006). Endocytosis and synaptic removal of NR3A-containing NMDA receptors by PACSIN1/syndapin1. Nat. Neurosci. *9*, 611–621. https://doi.org/10.1038/nn1680.

Perez-Otano, I., Schulteis, C.T., Contractor, A., Lipton, S.A., Trimmer, J.S., Sucher, N.J., and Heinemann, S.F. (2001). Assembly with the NR1 subunit is required for surface expression of NR3A-containing NMDA receptors. J. Neurosci. *21*, 1228–1237. https://doi.org/10.1523/JNEUROSCI.21-04-01228.2001.

Pfeffer, C.K., Xue, M., He, M., Huang, Z.J., and Scanziani, M. (2013). Inhibition of inhibition in visual cortex: the logic of connections between molecularly distinct interneurons. Nat. Neurosci. *16*, 1068–1076. https://doi.org/10.1038/nn.3446.

Pfisterer, U., Petukhov, V., Demharter, S., Meichsner, J., Thompson, J.J., Batiuk, M.Y., Asenjo-Martinez, A., Vasistha, N.A., Thakur, A., Mikkelsen, J., et al. (2020). Identification of epilepsy-associated neuronal subtypes and gene expression underlying epileptogenesis. Nat. Commun. *11*, 5038. https://doi.org/10.1038/s41467-020-18752-7.

Poulet, J.F.A., and Petersen, C.C.H. (2008). Internal brain state regulates membrane potential synchrony in barrel cortex of behaving mice. Nature *454*, 881–885. https://doi.org/10.1038/nature07150.

Reimer, J., Froudarakis, E., Cadwell, C.R., Yatsenko, D., Denfield, G.H., and Tolias, A.S. (2014). Pupil fluctuations track fast switching of cortical states during quiet wakefulness. Neuron *84*, 355–362. https://doi.org/10.1016/j.neuron.2014.09.033.

Rhomberg, T., Rovira-Esteban, L., Vikór, A., Paradiso, E., Kremser, C., Nagy-Pál, P., Papp, O.I., Tasan, R., Erdélyi, F., Szabó, G., et al. (2018). Vasoactive intestinal polypeptide-immunoreactive interneurons within circuits of the mouse basolateral amygdala. J. Neurosci. *38*, 6983–7003. https://doi.org/10.1523/JNEUROSCI.2063-17.2018.

Roberts, A.C., Díez-García, J., Rodriguiz, R.M., López, I.P., Luján, R., Martínez-Turrillas, R., Picó, E., Henson, M.A., Bernardo, D.R., Jarrett, T.M., et al. (2009). Downregulation of NR3A-containing NMDARs is required for synapse maturation and memory consolidation. Neuron *63*, 342–356. https://doi.org/10.1016/j.neuron.2009.06.016.

Rothman, J.S., Cathala, L., Steuber, V., and Silver, R.A. (2009). Synaptic depression enables neuronal gain control. Nature *457*, 1015–1018. https://doi.org/10.1038/nature07604.

Rothman, J.S., and Silver, R.A. (2018). NeuroMatic: an integrated open-source software toolkit for acquisition, analysis and simulation of electrophysiological data. Front. Neuroinform. *12*, 14. https://doi.org/10.3389/fninf.2018.00014.

Sakimura, K., Kutsuwada, T., Ito, I., Manabe, T., Takayama, C., Kushiya, E., Yagi, T., Aizawa, S., Inoue, Y., and Sugiyama, H. (1995). Reduced hippocampal LTP and spatial learning in mice lacking NMDA receptor epsilon 1 subunit. Nature *373*, 151–155. https://doi.org/10.1038/373151a0.

Saleem, A.B., Ayaz, A., Jeffery, K.J., Harris, K.D., and Carandini, M. (2013). Integration of visual motion and locomotion in mouse visual cortex. Nat. Neurosci. *16*, 1864–1869. https://doi.org/10.1038/nn.3567.

Sasaki, Y.F., Rothe, T., Premkumar, L.S., Das, S., Cui, J., Talantova, M.V., Wong, H.-K., Gong, X., Chan, S.F., Zhang, D., et al. (2002). Characterization and comparison of the NR3A subunit of the NMDA receptor in recombinant systems and primary cortical neurons. J. Neurophysiol. *87*, 2052–2063. https://doi.org/10.1152/jn.00531.2001.

Sheng, M., and Kim, E. (2011). The postsynaptic organization of synapses. Cold Spring Harbor Perspect. Biol. *3*, a005678. https://doi.org/10.1101/cshperspect.a005678.

Shibasaki, K., Hosoi, N., Kaneko, R., Tominaga, M., and Yamada, K. (2017). Glycine release from astrocytes via functional reversal of GlyT1. J. Neurochem. *140*, 395–403. https://doi.org/10.1111/jnc.13741.

Stringer, C., Pachitariu, M., Steinmetz, N., Carandini, M., and Harris, K.D. (2019b). High-dimensional geometry of population responses in visual cortex. Nature *571*, 361–365. https://doi.org/10.1038/s41586-019-1346-5.

Stringer, C., Pachitariu, M., Steinmetz, N., Reddy, C.B., Carandini, M., and Harris, K.D. (2019a). Spontaneous behaviors drive multidimensional, brainwide activity. Science *364*, 255. https://doi.org/10.1126/science.aav7893.

Stroebel, D., Mony, L., and Paoletti, P. (2021). Glycine agonism in ionotropic glutamate receptors. Neuropharmacology *193*, 108631. https://doi.org/10.1016/j.neuropharm.2021.108631.

Sucher, N.J., Akbarian, S., Chi, C.L., Leclerc, C.L., Awobuluyi, M., Deitcher, D.L., Wu, M.K., Yuan, J.P., Jones, E.G., and Lipton, S.A. (1995). Developmental and regional expression pattern of a novel NMDA receptor-like subunit (NMDAR-L) in the rodent brain. J. Neurosci. *15*, 6509–6520. https://doi.org/10.1523/JNEUROSCI.15-10-06509.1995.

Tang, W., Kochubey, O., Kintscher, M., and Schneggenburger, R. (2020). A VTA to basal amygdala dopamine projection contributes to signal salient somatosensory events during fear learning. J. Neurosci. *40*, 3969–3980. https://doi.org/10.1523/JNEUROSCI.1796-19.2020.

Tong, G., Takahashi, H., Tu, S., Shin, Y., Talantova, M., Zago, W., Xia, P., Nie, Z., Goetz, T., Zhang, D., et al. (2008). Modulation of NMDA receptor properties and synaptic transmission by the NR3A subunit in mouse hippocampal and cerebrocortical neurons. J. Neurophysiol. *99*, 122–132. https://doi.org/10.1152/jn.01044.2006.

Traynelis, S.F., Wollmuth, L.P., McBain, C.J., Menniti, F.S., Vance, K.M., Ogden, K.K., Hansen, K.B., Yuan, H., Myers, S.J., and Dingledine, R. (2010). Glutamate receptor ion channels: structure, regulation, and function. Pharmacol. Rev. *62*, 405–496. https://doi.org/10.1124/pr.109.002451.

Ulbrich, M.H., and Isacoff, E.Y. (2008). Rules of engagement for NMDA receptor subunits. Proc. Natl. Acad. Sci. USA *105*, 14163–14168. https://doi.org/10.1073/pnas.0802075105.

Wang, L., Tu, P., Bonet, L., Aubrey, K.R., and Supplisson, S. (2013). Cytosolic transmitter concentration regulates vesicle cycling at hippocampal GABAergic terminals. Neuron *80*, 143–158. https://doi.org/10.1016/j.neuron.2013.07.021.

Westergren, I., Nyström, B., Hamberger, A., Nordborg, C., and Johansson, B.B. (1994). Concentrations of amino acids in extracellular fluid after opening of the blood-brain barrier by intracarotid infusion of protamine sulfate. J. Neurochem. *62*, 159–165. https://doi.org/10.1046/j.1471-4159.1994.62010159.x.

Yaeger, C.E., Ringach, D.L., and Trachtenberg, J.T. (2019). Neuromodulatory control of localized dendritic spiking in critical period cortex. Nature *567*, 100–104. https://doi.org/10.1038/s41586-019-0963-3.

Yao, Y., and Mayer, M.L. (2006). Characterization of a soluble ligand binding domain of the NMDA receptor regulatory subunit NR3A. J. Neurosci. *26*, 4559–4566. https://doi.org/10.1523/JNEUROSCI.0560-06.2006.

Yuan, T., Mameli, M., O'Connor, E.C., Dey, P.N., Verpelli, C., Sala, C., Perez-Otano, I., Lüscher, C., and Bellone, C. (2013). Expression of cocaine-evoked synaptic plasticity by GluN3A-containing NMDA receptors. Neuron *80*, 1025–1038. https://doi.org/10.1016/j.neuron.2013.07.050.

Zeilhofer, H.U., Studler, B., Arabadzisz, D., Schweizer, C., Ahmadi, S., Layh, B., Bösl, M.R., and Fritschy, J.-M. (2005). Glycinergic neurons expressing enhanced green fluorescent protein in bacterial artificial chromosome transgenic mice. J. Comp. Neurol. *482*, 123–141. https://doi.org/10.1002/cne.20349.

Zhang, W.H., Herde, M.K., Mitchell, J.A., Whitfield, J.H., Wulff, A.B., Vongsouthi, V., Sanchez-Romero, I., Gulakova, P.E., Minge, D., Breithausen, B., et al. (2018). Monitoring hippocampal glycine with the computationally designed optical sensor GlyFS. Nat. Chem. Biol. *14*, 861–869. https://doi.org/10.1038/s41589-018-0108-2.

Zhu, Z., Yi, F., Epplin, M.P., Liu, D., Summer, S.L., Mizu, R., Shaulsky, G., Xiangwei, W., Tang, W., Burger, P.B., et al. (2020). Negative allosteric modulation of GluN1/GluN3 NMDA receptors. Neuropharmacology *176*, 108117. https://doi.org/10.1016/j.neuropharm.2020.108117.

STAR★METHODS

KEY RESOURCES TABLE

REAGENT or RESOURCE	SOURCE	IDENTIFIER
Antibodies		
Anti-GluN3A	Pr. Masahiko Watanabe; Marco et al., 2013	N/A
Nanogold-IgG goat anti-rabbit IgG	Nanoprobes	#2003
Bacterial and virus strains		
AAV9-CMV-EGFP-H1-shNR3A1185	Marco et al., 2018; Vector Biolabs	N/A
AAV9-GFP-H1-scrmb-shRNA	Marco et al., 2018; Vector Biolabs	N/A
AAV9-ENN-AAV-CaMKII.GCaMP6f-WPRE-SV40	Dr. James M Wilson, AddGene	Cat# 100834-AAV1; RRID: Addgene_100834
AAV9 Cag LSL tdTomato	Oh et al., 2014; AddGene	Cat#: 100048: RRID:Addgene_100048
AAV1-Ef1a-DIO-DSE-mCherry-PSEsh_scramble-WPRE-pA	This paper	N/A
AAV1-Ef1a-DIO-DSE-mCherry-PSEsh_GluN3A-WPRE-pA	This paper	N/A
Chemicals, peptides, and recombinant proteins		
D-AP5	Hello Bio	HB0225
NBQX disodium salt	Tocris/Hello Bio	Cat. No. 1044; HB0443
Picrotoxin	Abcam	Ab120315
NMDA	Hello Bio	HB0454
SR 95531 hydrobromide	Hello Bio	HB0901
5,7-Dichlorokynurenic acid 5,7-Dichlorokynurenic acid sodium salt	Tocris	0286; 3698
Dopamine hydrochloride	Sigma-Aldrich	H8502
CGP 78608 hydrochloride	Tocris	1493
Tetrodotoxin citrate	Hello Bio	HB1035
Strychnine hydrochloride	Sigma	S8753
Sarcosine	Tocris	2975
Alexa Fluor 594 hydrazide, sodium ium salt	Invitrogen	A10438
MNI-caged-L-Glutamate	Tocris	Cat. No. 1490
D-Serine	Sigma-Aldrich	S4250
Glycine	Sigma-Aldrich	G5417
EU1180-438	Zhu et al., 2020, Enamine	N/A
CNI-Glycine	This paper	N/A
Glycine Oxydase H244K	Creative enzymes/Bio Vision	NATE-1674 /7845
Bicuculline methochloride	Hello Bio	HB0895
Experimental models: Organisms/strains		
C57BL/6NRj	Janvier Labs Charles River	N/A
Ssttm2.1(cre)Zjh/J (SST-IRES-Cre)	Jackson Laboratory	RRID:IMSR_JAX:013044
Pvalbtm1(cre)Arbr/J (PV-Cre)	Jackson Laboratory	RRID:IMSR_JAX:008069
VIPtm1(cre)Zjh (VIP-IRES-Cre)	Jackson Laboratory	RRID:IMSR_JAX:010908
B6.Cg-Gt(ROSA)26Sortm9(CAG-tdTomato)Hze/J (td-tomato)	Jackson Laboratory	RRID:IMSR_JAX:007909
GAD65 EGFP	Wang et al., 2013	N/A
GluN3A KO	Das et al., 1998	N/A

(*Continued on next page*)

Continued

REAGENT or RESOURCE	SOURCE	IDENTIFIER
GluN2A KO	Sakimura et al., 1995	N/A
GluN1 Flox (NR1-2lox) mouse line	Niewoehner et al., 2007	N/A
Serine Racemase KO	Basu et al., 2009	N/A
Oligonucleotides		
pDIO-DSE-mCherry-PSEMCS and pDIO-DSE-mCherry-PSE-shLacZ	Favuzzi et al., 2019	N/A
shRNA targeting sequence: Grin3A 5'-CTACAGCTGAGTTTAGAAA-3'	Marco et al., 2018, Vector Biolabs	N/A
Grin3a riboprobe complementary to nucleotides 2853 to 3392 of mouse Grin3a mRNA	Pérez-Otaño et al., 2016	NM_001033351.2
vGlut2 riboprobe complementary to nucleotides 381-1491	Dr. Eduardo Puelles	NM_080853.3
Software and algorithms		
pClamp	Molecular Devices	RRID: SCR_011323
IGOR Pro 8	WaveMetrics	RRID: SCR_000325
Fiji	ImageJ	RRID: SCR_003070
GraphPad Prism 9	https://www.graphpad.com	RRID: SCR_002798
Affinity Designer	https://affinity.serif.com/fr/designer/	RRID: SCR_016952
Prairie View 5.4	Bruker	RRID: SCR_017142
Neuromatic	Rothman and Silver, 2018	http://www.neuromatic.thinkrandom.com/
EthoVision XT 14	Noldus	https://www.noldus.com/ethovision-xt

RESOURCE AVAILABILITY

Lead contact

Further information and requests for resources and reagents should be directed to and will be fulfilled by the Lead Contact Nelson Rebola (nelson.rebola@icm-institute.org).

Materials availability

The CNI-Glycine generated in this study can be made available upon request to Graham C.R. Ellis-Davies (graham.davies@mssm.edu).

Data and code availability

- All data reported in this paper will be shared by the lead contact upon request.
- Custom scripts used in this study have been deposited to a publicly accessible repository. The URL is listed in the key resources table.
- Any additional information required to reanalyze the data reported in this paper is available from the lead contact upon request.

EXPERIMENTAL MODEL AND SUBJECT DETAILS

Mice

Animals were housed in the Paris Brain Institute and IBENS rodent facilities accredited by the French Ministry of Agriculture. All experiments were performed in compliance with French and European regulations on care and protection of laboratory animals (EU Directive 2010/63, French Law 2013-118, February 6th, 2013), and were approved by local ethics committees and by the French Ministry of Research and Innovation (authorization numbers #05137.02, #28867 and #11199). For experiments performed in the BLA, male (behavior) or both male and female (electrophysiology) mice were used with corresponding littermates from the following lines: C57/B6, GluN2A KO (Sakimura et al., 1995), GluN3A KO (Das et al., 1998), SST-IRES-Cre X Ai9 (Gt(ROSA)26Sor$^{tm9(CAG-tdTomato)}$; JAX 007909), PV-Cre (Pvalb$^{tm1(cre)Arbr/J}$; JAX 008069) X Ai9 (Gt(ROSA)26Sor$^{tm9(CAG-tdTomato)}$; JAX 007909), GAD65 EGFP (Wang et al., 2013), all on a C57/B6 background. For experiments performed in the neocortex, both male and female mice were used with the following genotypes: SST-IRES-Cre (SST$^{tm2.1(cre)Zjh/J}$; JAX 013044); SST-IRES-Cre X Ai9

(Gt(ROSA)26Sor$^{tm9(CAG-tdTomato)}$; JAX 007909); PV-Cre (Pvalb$^{tm1(cre)Arbr/J}$; JAX 008069) X Ai9 (Gt(ROSA)26Sor$^{tm9(CAG-tdTomato)}$; JAX 007909); VIP-IRES-Cre (Vip$^{tm1(cre)Zjh/AreckJ}$; JAX 031628) X Ai9 (Gt(ROSA)26Sor$^{tm9(CAG-tdTomato)}$; JAX 007909); SST-IRES-Cre (SST$^{tm2.1(cre)Zjh/J}$; JAX 013044) X Serine Racemase KO (Basu et al., 2009); SST-IRES-Cre (SST$^{tm2.1(cre)Zjh/J}$; JAX 013044) X GluN1 Flox (Niewoehner et al., 2007); SST-IRES-Cre (SST$^{tm2.1(cre)Zjh/J}$; JAX 013044 X GluN3A KO. Animals were maintained on a 12-hour light/dark cycles with food and water provided *ad libitum*.

METHOD DETAILS

Slice preparation

Amygdala

Adult (>2 months old) mice were deeply anesthetized with isoflurane before decapitation. The brain was quickly removed and immerged in an ice-cold artificial cerebrospinal fluid (ACSF) containing (in mM): 115 NaCl; 3.3 KCl; 25.5 Na_2HCO_3; 1.2 Na_2HPO_4; 25 Glucose; 1 $MgSO_4$; 2 $CaCl_2$ and 0.5 of Ascorbic Acid. The ACSF solution was continuously bubbled with a 95% O_2/ 5% CO_2 mix, equilibrating the pH at 7.3-7.4. Coronal brain slices (300-320 μm) containing the amygdala were cut using a 7000 SMZ-2 Vibrotome (Campden Instruments Ltd, UK) in ice-cold ACSF. Slices were then transferred for 30 minutes in warm ACSF (34°C) before placing them for the rest of the experimental day in ACSF at room temperature.

Cortex

Mice (>P25) were anesthetized with a mix of i.p. ketamine (100mg/kg) and xylazine (13 mg/kg). The animals were briefly transcardially perfused (approximately 3 min) with ice-cold sucrose-based ACSF composed of (in mM): 220 Sucrose, 2.5 KCl, 0.5 $CaCl_2$, 7 $MgSO_4$, 11 Glucose, 26 $NaHCO_3$, 0.125 NaH2PO_4, continuously bubbled with carbogen (95% O_2/ 5% CO_2). Brains were subsequently removed and parasagittal slices of 320 μm were obtained using a vibratome (Leica VT1200S). Brain slices were allowed a 10 minutes recovery period in oxygenated ACSF containing (in mM): 126 NaCl, 0.25 KCl, 1.5 or 2 $CaCl_2$, 1.5 or 1 $MgCl_2$, 15 Glucose, 26 $NaHCO_3$, 0.125 NaH_2PO_4.H_2O, at 34°C and an additional 20 minutes at room temperature before starting recordings.

Spinal cord

Similarly to cortex, mice (P>25) were anesthetized with a mix of i.p. ketamine (100 mg/kg) and xylazine (13 mg/kg). The animals were transcardially perfused for approximately 3 min with ice-cold sucrose-based Artificial Cerebral Spinal Fluid (ACSF) composed of (in mM): 220 Sucrose, 2.5 KCl, 0.5 $CaCl_2$, 7 $MgSO_4$, 11 Glucose, 26 $NaHCO_3$, 0.125 NaH_2PO_4, continuously bubbled with carbogen (95% O_2/ 5% CO_2). The spinal cord was extracted by laminectomy and 300 μm parasagittal slices were obtained. The slices were allowed a 10 minutes recovery period in oxygenated ACSF containing (in mM): 126 NaCl, 0.25 KCl, 1.5 or 2 $CaCl_2$, 1.5 or 1 $MgCl_2$, 15 Glucose, 26 $NaHCO_3$, 0.125 NaH_2PO_4.H2O, at 34°C and an additional 20 minutes at room temperature before starting recordings.

Ex vivo electrophysiology

For electrophysiological recordings in amygdala, brain slices were moved to a recording chamber on an Olympus BX51WIF microscope (Olympus, France) and continuously perfused with oxygenated ACSF (3-4 mL/min; 30-34°C). Recorded neurons were located in the basolateral part of the amygdala and were visually identified using a Qimaging RETIGA 2000R camera (Teledyne Photometrics, USA) run by Micro-Manager (Vale Lab, USCF, USA). For whole-cell experiments, except for the NMDA puffs, patch pipettes (3-5 MΩ tip resistance) were filled with an intracellular solution containing (in mM): 130 K-Gluconate; 0.6 EGTA; 2 $MgCl_2$; 0.2 $CaCl_2$; 10 HEPES; 2 Mg-ATP; 0.3 Na_3-GTP, pH 7.3 with KOH (295-300 mOsm). For the NMDA puffs, the patch pipettes were filled with (in mM): 120 $CsMeSO_3$; 10 HEPES; 4.6 $MgCl_2$; 10 K_2-creatine phosphate; 15 BAPTA; 4 Na_2-ATP; 0.4 Na_2-GTP, 0.05 4-AP and 10 TEA-Cl. Whole-cell and cell-attached recordings were carried out using a Multiclamp 700B amplifier (Molecular Devices, United Kingdom) run by the Multiclamp 700B interface. In the whole-cell configuration, series resistances were compensated up to 65% maximum.

Recordings in the neocortex were performed on neurons located in L2/3 of the primary somatosensory cortex (barrel field; 3-5 MΩ tip resistance). In spinal cord slices, neurons were recorded in the dorsal horn of the spinal cord within the lumbar segment. Cells were visually identified in a Olympus BX51WIF or BX61WIF microscope (Olympus, France) using a INFINITY 3S-1URM CCD camera (Teledyne Lumenera, Canda) run by Infinity Capture software (Teledyne Lumenera, Canada). Brain slices were continuously perfused with oxygenated ACSF (30-34°C). For voltage-clamp experiments, a cesium based intracellular solution was used (in mM): 100 Cesium Methanesulphonate, 10 BAPTA, 10 HEPES, 10 TEA-Cl, 5 QX314, 4 $MgCl_2$, 2 $CaCl_2$, 4 $ATPNa_2$, 0.3 GTPNa (pH = 7.4, 290 mOsm). Globally, cells were maintained at -60 mV except for NMDA/AMPA ratio estimation where the holding voltage varied from -70 mV to +40 mV. For current clamp recordings, a K^+-based intracellular solution was used (in mM): 135 K-D-gluconate, 5 KCl, 10 HEPES, 0.01 EGTA, 10 Na_2 phosphocreatine, 4 MgATP, 0.3 NaGTP (pH = 7.4, 290 mOsm). For both intracellular solutions, values were not corrected for liquid junction potential. Recordings were carried out using a Multiclamp 700B (Molecular devices, United Kingdom) run by the Multiclamp 700B interface. The current traces were filtered with a 10kHz Bessel filter and digitized at 100 kHz using an analog-to-digital converter (model NI USB 6363, National Instruments, Austin, TX, USA). Data acquisition was performed with Igor Pro software and Neuromatic extension (https://www.wavemetrics.com/).

For all loose-cell attached recordings, pipettes were filled with either K-Gluconate intracellular solution or HEPES-buffered solution containing (in mM): 150 NaCl; 2.5 KCl; 1.25 NaH_2PO4; 10 HEPES; 2 $CaCl_2$; 1 $MgCl_2$; pH 7.35 with NaOH (~305 mOsm).

For puff experiments, Glycine (10 mM) or NMDA (1 mM) were puffed locally at the surface of the slice near the recorded cell through a pipette (2-3 MΩ tip resistance; 1000-5000 msec puff duration) with a pneumatic drug ejection system [PicoPump PV 820 (WPI, Germany) or PDES-02DX (NPI electronics, Germany). During glycine puff experiments, puff pipettes contained antagonists of $GABA_A$ (10 μM Bicuculine), glycine (20 μM strychnine), AMPA (10 μM NBQX) and NMDA (50 μM D-AP5) receptors as well as TTX (200 nM). For NMDA puffs, strychnine and D-AP5 were omitted from the puff solution and mecamylamine hydrochloride (10 μM) was added to the bath solution. D-AP5 was also present in the bath of all voltage-clamp experiments performed to probe variations in holding currents.

Extracellular synaptic stimulation was obtained by applying extracellular voltage pulses (50 ms, 5-50 V; Digitimer Ltd, UK or A-M systems, USA) delivered using a second patch pipette filled with ACSF or HEPES-buffered solution. The stimulating pipette was placed within the vicinity of the cell body (neocortex) or external capsule (BLA). In S1 SST-INs, glutamatergic inputs were stimulated with a paired-pulse protocol (50 ms interpulse interval) to increase basal release probability that is particularly low at these synapses. To estimate NMDA/AMPA current amplitude ratio AMPAR-EPSCs were recorded at a holding potential of -70 mV while NMDAR-EPSCs current were recorded at a holding potential of +40mV (S1 SST-INs) or +60 mV (BLA PNs) in the presence of NBQX (10 μM). For SST-INs NMDA/AMPA ratio was calculated taking the amplitude of the second pulse of the paired-pulse stimulation protocol. To probe changes in excitability of BLA PNs, a stimulation pipette was placed over the external capsule while APs were recorded from PNs in the cell-attach configuration.

Synthesis of CNI-Glycine (CNI-Gly)

Synthesis of CNI-Gly followed procedures previously developed for caging glutamate and GABA (Ellis-Davies, 2011). All chemicals were purchased from commercial sources and used as received unless otherwise noted. Reactions were monitored by thin-layer chromatography (TLC) on Merck KGaA glass silica gel plates (60 F254) and were visualized with UV light. NMR spectra were recorded on a Varian 300 MHz NMR spectrometer. The chemical shifts are reported in ppm using the solvent peak as the internal standard. Peaks are reported as: s = singlet, d = doublet, t = triplet, q = quartet, dd = doublet of doublets, m = multiplet. High resolution mass spectral data were obtained using an Agilent G1969A ToF LC-MS (Agilent, Santa Clara, CA, USA).

Reverse-phase chromatography used two systems. Analytical UPLC was carried out with a Waters Acuity Arc (Milford, MA, USA) using a BEH300 C-18 column (2 × 50 mm, 1.7 μm particle size) monitored with a 2998 PDA detector. Elution used a linear gradient elution (0-100% acetonitrile, in water with 0.1 % TFA for 6 min). Preparative HPLC was carried out using a Waters PrepLC using an Alltech Altima C-18 column (22 x 250 mm, 5.0 μm particle size) monitored with a 2489 detector at 254 nm. Isocratic elution was used (10 mL min^{-1}) with 25% MeCN in water with 0.1% TFA.

Compound 3

To a solution of **2** (Figure S3; 0.038 g, 0.18 mmol), EDC (0.070 g, 0.28 mmol) in MeCN (10 mL) was added BOC-glycine (0.050 g, 0.25 mmol). The reaction mixture was stirred at RT for 40 h. The solvent was removed under reduced pressure, then 1N HCl (10 mL) and ethyl acetate (40 mL) was added to the reaction mixture. The aqueous layer was separated, and the organic phase was washed with a saturated sodium bicarbonate solution (10 mL). The organic phase was dried with $MgSO_4$, concentrated under reduced pressure to give **3** (0.057 g, 0.157 mmol) in a 86% yield. ^{1}H NMR (300 MHz, $CDCl_3$): δ = 7.84 (d, J = 8.1 Hz, 1H), 7.15 (t, J = 8.1 Hz, 1H), 6.46 (d, J = 8.1 Hz, 1H), 5.57 (br s, 1H), 4.67 (s, 2H), 4.02 (t, J = 6.4 Hz, 2H), 3.79 (s, 2H), 3.23 (t, J = 6.4 Hz, 2H), 1.46 (s, 9H). ^{13}C NMR (75 MHz, $CDCl_3$): δ = 169.3, 166.5, 155.8, 154.1, 144.1, 130.0, 129.1, 119.1, 113.8, 110.8, 107.3, 79.8, 77.2, 65.3, 52.3, 52.2, 47.2, 47.1, 43.9, 28.3, 25.3. HRMS: m/z calcd for C18H24N2O6 requires 364.1634, 365.1713 M+H found

Compound 1

To a solution of **3** (0.057 g, 0.157 mmol) in methanol (30 mL) was added 1N NaOH (0.235 mL), and the reaction was stirred at RT for 3 h. Most of the methanol was removed under reduced pressure, then ethyl acetate (40 mL) and 1N citric acid (5 mL) were added to the reaction mixture. The organic phase was separated, dried with $MgSO_4$, then concentrated under reduced pressure to give **4**, which was pure enough for the next step (HRMS: m/z calcd for C12H14N2O4 requires 350.1478, 351.1552 M+H found). Acid 4 (ca. 0.25 mmol) was dissolved in TFA (10 mL) and stirred at RT. HPLC analysis revealed complete deprotection of **4** to amine **5** after 60 min. To this solution $NaNO_3$ (0.051 g, 0.6 mmol) was added, and the reaction mixture was stirred at RT for 30 mins, after which UPLC analysis revealed **5** had reacted completely to give a mixture of **1** and the analogous 5-nitro isomer. The TFA was removed in a fumehood under a flow of compressed nitrogen, followed by high vacuum. The mixture was dissolved in water with 25% MeCN, and 0.1% TFA, filtered through Celite, then a 0.45 micron nylon filter to give a clear, dark brown solution. This was purified by preparative HPLC. The organic phase was removed under reduced pressure, the resultant aqueous solution frozen, then lyophilized to give the TFA salt of **1** (0.011 g, 0.027 mmol) as a cream solid in a 9.5% yield. ^{1}H NMR (300 MHz, MeOD): δ = 7.75 (dd, J = 9.2 Hz, dd), 6.83 (dd, J = 9.2 Hz, dd), 4.85 (s, 2H), 4.26 (t, J = 7.1 Hz, 2H), 4.20 (s, 2H), 3.23 (t, J = 7.1 Hz, 2H). ^{13}C NMR (75 MHz, MeOD): δ = 164.2, 157.6, 135.5, 124.8, 123.9, 108.3, 63.0, 48.9, 40.9, 26.0. HRMS: m/z calcd for C12H13N3O6 requires 295.0804, M+H 296.0876 found.

Quantum yield measurement

UV-Vis absorption spectra were recorded using a Cary 50 spectrophotometer (Agilent). Photolysis used a 365 nm LED (M365LP1, Thorlabs, Sparta, NJ, USA) in HEPES buffer (40 mM, 100 mM KCl, pH 7.4) in a quartz cuvette (1 cm pathlength). Solutions of CNI-Gly and MNI-Glu having matching absorptions at 365 nm (concentrations ca. 0.05 mM) were irradiated over a period of 6 min. Changes in the absorption spectra of CNI-Gly and MNI-Glu were taken every 60 s.

Comparison of CNI-Gly quantum yield to other caged compounds

The photochemistry of 7-nitro-indolinyl caged neurotransmitters is well characterized (Matsuzaki et al., 2010; Papageorgiou and Corrie, 2000). Irradiation with near-UV light releases the caged neurotransmitter, along with a nitroso-indole "spent cage". The latter shows a distinct bathochromic shift when compared to the indoline starting material. This absorption change has been shown to correlate with amino acid release quantitatively (Papageorgiou and Corrie, 2000). Thus, the time course of photolysis of CNI-Gly was compared to MNI-Glu, which has a quantum yield of 0.065 (Corrie et al., 2016). CNI-Gly was found to photolyze about 1.5x faster in the initial time domain, corresponding to a quantum yield of photolysis of 0.10 (n=3). This quantum yield is the same as CNI-GABA (Matsuzaki et al., 2010).

Uncaging Experiments

For two-photon uncaging experiments caged compounds were locally applied (5 mM CNI-Gly and 10 mM MNI-Glu, Tocris Bioscience for MNI) via a patch pipette (~2-3 μm tip diameter) placed within 15-20 μm of dendrites/somas. The local perfusion solution contained (in mM): 125 NaCl, 2.5 KCl, 10 HEPES, 2 $CaCl_2$, 1 $MgCl_2$, 1.25 NaH_2PO_4, 25 glucose, and 1 μM CGP-78608. For CNI-Gly photolysis experiments, the extracellular solution contained antagonists of $GABA_A$ (10 μM Bicuculine), glycine (20 μM strychnine, Sigma) and AMPA (10 μM NBQX) receptors as well as 1 μM CGP-78608. For MNI-glutamate, antagonists of AMPA and NMDA receptor were removed. BLA PNs and SST-INs were held at -60 mV in voltage-clamp configuration throughout uncaging experiments, while for spinal cord neurons (Figures S4A–S4C) membrane potential was clamped at 0 mV.

The output of two pulsed Ti:Sapphire (DeepSee, Spectraphysics) lasers were independently modulated to combine uncaging of MNI-glutamate and 2P imaging of patch-labelled (Alexa 594 10 μM) neurons. The imaging laser beam was tuned to 840 nm and modulated using a Pockels cell (Conoptics, Danbury, CT). For uncaging, the intensity and duration (1-20 ms) of illumination of the two-photon laser beam tuned to 720 nm was modulated using an acousto-optic modulator (AA Opto-Electronic, France). Parfocality of the two wavelengths was verified using bleached spots on a microscope slide coated with fluorescent ink. Photolysis laser power, estimated at the exit of the objective were <20 mW. Uncaging spots were positioned 1μm away from targeted location to reduce direct illumination of cellular compartments. For full-field one-photon CNI-Glycine uncaging (Figure S3G) a 405 nm LED (CAIRN research, UK) was used and mounted on the epifluorescence port of a BX51 microscope (Olympus, Japan). The light was directed to the objective by a standard long-pass dichroic (488 nm, Semrock, Rochester, NY, USA) in the fluorescence turret. Light power was controlled via the LED driver (OPTOLED LITE, CAIRN research, UK) by external voltage modulation.

Fluorescence *in situ* hybridization (FISH)

Wild-type (WT) and $GAD67^{GFP}$ (B6.Cg-Tg[Gad1-EGFP]) mice (C57BL/6J background) were transcardially perfused with 4% paraformaldehyde in PBS. Brains were removed, post-fixed overnight at 4°C, embedded in 4% agarose and cut in a vibrating microtome. Briefly, free-floating 80 μm-thick brain sections were permeabilized, and incubated with digoxigenin- and fluorescein-labeled riboprobes (against *Grin3a* and *vGlut2* mRNA, respectively) at 63°C in hybridization buffer overnight. Hybridized probes were detected using peroxidase-conjugated anti-digoxigenin or anti-fluorescein antibodies (Roche 11 207 733 910 and Roche 11 426 346 910 respectively, 1:2000) in blocking solution overnight at 4°C. TSA plus fluorescence kit was used for signal amplification and detection according to the manufacturer protocol (ThermoFisher, NEL744001KT). FISH in $GAD67^{GFP}$ sections was performed via incubation with digoxigenin-labeled riboprobe alone. After the FISH procedure, sections were processed for GFP immunofluorescence to amplify the signal. Double FISH in C57BL/6J WT brain sections was performed with dual hybridization and duplication of detection and amplification steps. Sections were mounted onto Superfrost Plus slides, air-dried and coverslipped with fluorescence mounting medium (DAKO). Confocal images were captured on an Olympus FV1200 with a 20X objective and processed with FV10-ASW_Viewer software.

Immunoelectron microscopy

Immunohistochemical reactions were carried out using the post-embedding immunogold technique. Briefly, ultrathin sections 80 nm thick from Lowicryl-embedded blocks of BLA from P21-P30 mice were picked up on single slot coated nickel grids and incubated on drops of a blocking solution consisting of 2% Human Serum Albumin (HSA) in 0.05 M TBS and 0.03% (v/v) Triton X-100 (TBST). The grids were incubated with anti-GluN3A antibody (Marco et al., 2013; 10 μg/ml) at 28°C overnight and then on drops of goat anti-rabbit IgG conjugated to 10 nm colloidal gold particles (Nanoprobes) in 2% (w/v) HSA in TBST. The specificity of the anti-GluN3A antibody was previously assessed by the absence of signal in samples from GluN3A KO mice (Marco et al., 2013; Otsu et al., 2019). Finally, the grids were washed in TBS and counterstained for electron microscopy with saturated aqueous uranyl acetate followed by lead citrate. Ultrastructural analyses were performed in a Jeol-1010 (Tokyo, Japan) electron microscope and image acquisition was done using a digital Gatan camera ES100W model 785 (Gatan, Inc., Pleasanton, CA, USA). The numbers of gold particles associated with postsynaptic densities (PSD), along the extrasynaptic plasma membrane or in intracellular sites, were counted and the percentage of gold particles in the sub-compartments was calculated.

Viral injections

Adult male C57/B6 mice were bilaterally infused in the basolateral amygdala with either AAV2/9-shRNA-GluN3A-EGFP or AAV2/9-scramble-EGFP (200-300 nL at 0.05-0.1 μL/min). The following coordinates relative to Bregma were used: anterior-posterior [AP],

-1.35/-1.38mm; medial lateral [ML], ± 3.41/3.43 mm. The dorso ventral [DL], -4 mm coordinate was chosen relative to brain surface. Following the injection, the needle was left in place for 5 minutes to allow full diffusion of the viruses. All experiments (*ex vivo* electrophysiology and behavioral experiments) were performed at least 2 weeks after the surgery.

To reduce expression of GluN3A subunits selectively in SST-INs, Cre-dependent shRNA constructs (AAV1-Ef1a-DIO-DSE-mCherry-PSEsh_scramble-WPRE-pA or AAV1-Ef1a-DIO-DSE-mCherry-PSEsh_GluN3A-WPRE-pA) were infected in the barrel cortex of SST-Cre mice (320 nL at 0.06 μL/min). Stereotaxic coordinates were measured from the midline and from bregma (lateral of midline/posterior of bregma/depth in mm): Barrel cortex (3.1/0.5-1/0.2-0.35). To visualize SST-INs in SST-IRES-Cre X GluN1-floxed mice, injection of AAV9-CAG-LSL-tdTomato (Addgene; Plasmid #100048) was performed in S1 at least two weeks before electrophysiological recordings. For calcium imaging experiments, mice were homozygous for Cre and in addition to the shRNA constructs were also injected with AAV9-ENN-AAV-CaMKII.GCaMP6f-WPRE-SV40 (Addgene; Plasmid #100834) in order to express the genetically-encoded calcium indicator GCaMP6f mainly in pyramidal cells. pAAV.CAG.LSL.tdTomato was a gift from Hongkui Zeng (Addgene plasmid # 100048; http://n2t.net/addgene:100048 and pENN.AAV.CamKII.GCaMP6f.WPRE.SV40 was a gift from James M. Wilson (Addgene viral prep # 100834-AAV9; http://n2t.net/addgene:100834).

In vivo two-photon calcium imaging

Surgery

Mice were anaesthetized with 2% isoflurane and placed into a stereotaxic frame. The body temperature of the mice was monitored and kept constant. Mice were kept on a thermal blanket, and their eyes were protected with artificial tear ointment. The skin above the skull was disinfected with povidone iodine. A craniotomy was made over the right barrel cortex (3 mm in diameter) using a biopsy punch and sealed with a glass coverslip (CS-3R Warner Instruments). A metal headplate (Luigs and Neuman) and the glass coverslip were then glued in place using dental cement (Superbond). Mice were allowed to recover for at least 2 weeks before doing habituation. Mice were habituated to the imaging setup by handling and training for 4-6 d.

Two-photon imaging

In vivo imaging was performed with an Ultima IV two-photon laser-scanning microscope system (Bruker), using a 20×, 1.0 N.A. water immersion objective (Olympus) with the femtosecond laser (MaiTai DeepSee, Spectra Physics) tuned to 920 nm for imaging of cells expressing GCaMP6f or GCaMP6s and to 1020 nm for imaging of cells expressing mCherry. Fluorescence light was separated from the excitation path through a long pass dichroic (660dcxr; Chroma, USA), split into green and red channels with a second long pass dichroic (575dcxr; Chroma, USA), and cleaned up with band pass filters (hq525/70 and hq607/45; Chroma, USA). Fluorescence was detected using epifluorescence photomultiplier tubes (gallium arsenide phosphide, H7422PA-40 SEL, Hamamatsu). Time-series movies of neuronal populations expressing GCaMP6f were acquired at the frame rate of 30Hz (512 × 512 pixels field of view; 1.13 μm/pixel). Time-series were only recorded when a signal was present in the red channel, indicating the presence of infected SST cells in the vicinity. The duration of each focal plane movie was 300s (9000 frames) to track spontaneous neuronal activity. During the recording periods animals were free to run in a circular treadmill. Locomotion was monitored using a rotary encoder (H5-1000-NE-S, US Digital) and digitized with analog-to-digital converter (model NI USB 6363, National Instruments, Austin, TX, USA) at 2000 Hz.

Behavioral experiments

Mice used for behavioral experiments were 8 weeks old at the time of viral injection. They were housed (4 animals per cage) under standard conditions with food and water available *ad libitum* and a 12h light/dark cycle. After completion of the experiments, sites of injection were systematically verified and only mice correctly injected were kept for analysis.

Anxiety tests

Open field test

To evaluate locomotor activity and anxiety-like behavior, mice were placed in a circular arena (38 cm diameter, Noldus) and video-tracked from above. The position of the center point of the mice was tracked with Ethovision XT 14 and the distance moved, time in the center area, frequency of entries in the center area, were analyzed for a 10 min period.

Elevated plus maze

Mice were placed in the center zone (6 x 6 cm), facing an open arm of an elevated plus maze (Noldus, elevated 52 cm above the floor) with 2 open arms (36 cm length, 6 cm width) and 2 wall-enclosed arms (closed arms, 36 cm length, 6 cm width, walls 25 cm high) and let explore freely for 5 minutes. Mice were videotracked using Ethovision XT 14, and the amount of time spent and distance moved in the open arms, closed arms and center zone were analyzed.

Light-dark box

Mice were placed in the light zone and let explore the light-dark arena (Noldus) freely for 5 minutes. Light zone consisted in an area of 40 cm x 20 cm, 150 lux, while the dark zone was 20 x 20 cm, 0 lux. Their path was video tracked in the light and dark zones using Ethovision XT 14 and the amount of time spent in the light versus dark zones and distance travelled in the light zone were analyzed.

Pavlovian fear conditioning and extinction

Pavlovian fear conditioning and extinction training were performed in a sound-attenuating chamber (Ugo Basile) and the stimuli presentation were controlled by the Ethovision XT 14 (Noldus). Fear conditioning was carry out in a context A, which consisted in a 17x17x25 cm chamber with black/white-checkered walls and a grid floor, with peppermint-soup odor, cleaned with a 70 % ethanol within mice. Following an acclimation period of 180 s, mice received 5 pairings of a 30 s, 80 dB, 2.7 kHz tone (conditioned stimulus, CS) with a 0.5 s, 0.4 mA electrical footshock (unconditioned stimulus, US), in which the US was presented co-terminating with the CS. Each CS-US pairing was followed by a 120 s inter-pairing interval, and after the last 120 s no-stimulus period following the final CS-US pairing mice were returned to the home cage. For experiments in Figures 7A and 7B, mice were sacrificed just after the last 120s no-stimulus period following the final CS-US pairing. Brains were removed and slices were obtained as described above (see slice preparation and ex vivo electrophysiology). Twenty-four hours after fear conditioning, recall of the fear response to the CS and the first extinction training were performed. Mice were placed in a novel context B: chamber with yellow semi-transparent cylindrical wall, a solid-Plexiglas, opaque floor, and vanilla-extract solution to provide a distinctive olfactory cue. The chamber was cleaned with the disinfectant detergent solution Surfa'safe premium (Anios) between trials. Following an initial 180 s acclimation period, the mouse received 25 × 30 s presentations of the CS (30 s no-stimulus interval). The second and third extinction sessions took place in the next two days under the same conditions.

Mice were videotracked using Ethovision XT 14 during all the trial. Freezing behavior (immobility except for respiration movements) was assessed by the inactive periods, defined as periods of time during which the average pixel change of the entire video image was less than 0.5 % (from one video frame to another) and the threshold was fixed avoiding the detection of the breathing movements. Freezing behavior was analyzed during each CS presentation and during the habituation period in the context A and B.

Drugs and enzyme

With the exception of glycine and NMDA, all the drugs were bath applied: D-AP5 (HelloBio), NBQX (HelloBio or Tocris), Bicuculline (HelloBio or Tocris), Gabazine (Tocris), Picrotoxin (abcam), Strychnine (Sigma), TTX (HelloBio or Tocris), CGP-78608 (Tocris), 5,7-Dichlorokynurenic acid (DCKA; Tocris), Sarcosine (Sigma), D-serine (Sigma), CNQX (Tocris), mecamylamine (Sigma). Dopamine (Sigma), 1,4-Dithioerythritol (DTE) (Sigma). For enzymatic treatment, slices were incubated for at least 40 min with glycine oxidase H244K (0.03 U/ml, Creative enzymes or 0.06 U/ml, Biovision) to optimally degrade glycine and then continuously perfused with ACSF containing the enzyme during the experiment. For Dopamine and DTE treatments, slices were incubated for at least 1 hr with either dopamine (60 μM) or DTE (3 mM). Regarding dopamine, slices were then continuously perfused with ACSF containing dopamine during the rest of the experiment.

QUANTIFICATION AND STATISTICAL ANALYSIS

Analysis of *ex vivo* electrophysiological recordings

Data analysis was performed with the following software: pClamp 10 (Molecular Devices, USA), ImageJ (NIH, USA), Igor (WaveMetrics, USA), Excel (Microsoft Office) and GraphPad Prism. For electrophysiological recordings peak amplitudes of evoked EPSCs were measured as the difference between the baseline level immediately preceding the stimulation artifact or the puff application and the mean amplitude over a 1-5 ms window centered on the peak of the response. *n* indicates the number of different recorded cells. Displayed traces for EPSCs are averages of >3 trials for puff- or photolysis-evoked responses and >20 trials for synaptic currents. For experiments investigating tonic eGlyRs activity, holding currents were probed at 0.1 Hz from individual cells and extracted from individual voltage-clamp traces as the average current over a 1s window. To calculate the effects of the different pharmacological manipulations in holding currents an average baseline value (3 min window) was subtracted from the average value obtained after a 10 min drug application period. In Figures 2A and 2B, current-voltage (I-V) relationships values were normalized to the current amplitude obtained at +40 mV or +50 mV for cortex and BLA respectively.

Intrinsic properties of SST-INs (Figure 5) were measured in current-clamp conditions and calculated from 1-s-long current injection step. The resting membrane potential (in mV) was measured with 0 pA current injection 5 min after entering in whole-cell access. Currents steps were applied at the Vrest. Plots of spiking frequency in function of injected current were fit with the following Hill equation (adapted from Rothman et al., 2009):

$$F(I) = \frac{Fmax}{1 + \left(\frac{I_{50}}{I}\right)^{n}} \quad \text{(Equation 1)}$$

where, n is the exponent factor, *F*max is the maximum firing rate and I_{50} is the value of *I* at which *F* reaches half maximum. Fits were applied to data obtained from individual cells and rheobase was estimated as the current value required to reach 5% of Fmax and gain as the slope between 5% and 75% of the maximum value. Input resistance (Ri) was estimated as the slope of the current to

voltage relationship obtained upon the injection of −30, 0 and 30 pA to cells kept at resting potential. Membrane time constant was estimated fitting the time course of Vmemb after the injection of a 1 s, −30 pA current step. The first action potential evoked at rheobase was taken to measure amplitude, width and threshold. Threshold was considered as the potential at which dV/dt reached 10 mV/ms; amplitude was the difference between peak amplitude and threshold and half-width was the time interval between rise and decay phase measured at 50% of amplitude.

Two-photon data analysis

Raw fluorescence time-series movies were analyzed using the Suite2p toolbox (Pachitariu et al., 2017), available at https://github.com/cortex-lab/Suite2P. The Suite2p pipeline consists of registration, cell detection, region of interest (ROI) classification, neuropil quantification as well as spike deconvolution. In short, Suite2P first aligns all frames of a calcium movie using two-dimensional rigid registration based on regularized phase correlation, subpixel interpolation, and kriging. In all recordings, the registered movie was visually inspected and if clear Z-movements were present, the movie was excluded from analysis. To detect ROIs (corresponding to cells), Suite2p clusters correlated pixels. The number of ROIs is determined automatically by a threshold on pixel correlations. These ROIs were then manually curated so that only somas were detected. GCaMP6f signals were further processed using custom Python 3.7 code. Fluorescence traces from each ROI was corrected for neuropil contamination by subtracting from each ROI signal the surrounding neuropil signal scaled by a factor of 0.7 like previously reported (Stringer et al., 2019b). After neuropil subtraction, changes in fluorescence were quantified as $\Delta F/F_0$. Baseline fluorescence (F_0) was calculated by filtering the fluorescence trace (F) using a 60s gaussian filter followed by a minimum and maximum sliding window of 60 seconds. This type of baseline calculation was used to remove long time scale drifts in baseline.

Analysis of Ca^{2+} imaging during periods of locomotion

Changes in the position on the circular treadmill were down sampled to 30 Hz using linear interpolation matching the sampling rate of the two-photon imaging. Periods of locomotion were defined as periods where the instantaneous speed was $\geq$ 0.1 cm/s and if speed was <0.1 cm/s was defined as resting. Periods including 0.5 s before and 2.5 s after locomotion periods were not included in analysis. Sessions where the percentage of locomotion or resting periods were <5% were also excluded from analysis. Locomotion modulation index (LMI) as defined as the difference between the mean $\Delta F/F_0$ during running periods (F_{run}) and resting periods (F_{rest}), divided by the sum of the two ($LMI=(F_{run} - F_{rest})/(F_{run} + F_{rest})$).

Confocal imaging data acquisition and analysis

Two weeks after injection of AAV2/9-shRNA-GluN3A-EGFP, SST-tdtomato or PV-tdtomato mice (see key resources table) were sacrificed and perfused with PFA 4%. Brains were dissected, sliced at 80 μm, labeled with DAPI (1/1000) and mounted on microscope slides. Images were acquired using an SP8 LEICA confocal microscope with a 40X objective. Images were analyzed using ImageJ. Red and/or green fluorescent cells were manually quantified and reported as percentage of total amount of cells.

Statistical analysis

All data are presented as mean ± standard error of the mean (SEM). For statistical comparisons non-parametric tests were used (Kruskal-Wallis followed by Dunn's multi-comparison test, Mann-Whitney U and Wilcoxon test). In some datasets following a normal distribution (Shapiro–Wilk test) paired/unpaired t-tests or two-way ANOVA test were also used. P values are reported in the figure legends according to the following star symbols: *P<0.05, **P<0.01, ***P<0.001, ****P<0.0001. Statistical significance was set for P values below 0.05. n.s. for 'not significant'.